Synthetic control of actin polymerization and symmetry breaking in active protocells

Shiva Razavi 1,2,†* , Felix Wong 3,4 , Bedri Abubaker-Sharif 1,2 , Hideaki T. Matsubayashi 2 , Hideki Nakamura 2§ , Nhung Thi Hong Nguyen 2 , Douglas N. Robinson 2,5 , Baoyu Chen 6 , Pablo A. Iglesias 1,2,7 , and Takanari Inoue 1,2*

- † Present address: Institute for Medical Engineering & Science, Department of Biological Engineering, MIT, Cambridge, MA 02139, USA.
- § Present address: Kyoto University Graduate School of Engineering, Department of Synthetic Chemistry and Biological Chemistry, Katsura Int'tech Center, Graduate School of Engineering, Kyoto University, Nishikyo-ku, Kyoto, 615-8530, Japan.

Summary We built a protocell that senses a directed or undirected external chemical input and self-organizes its actin cytoskeleton to break symmetry.

¹ Department of Biomedical Engineering, Johns Hopkins University School of Medicine, Baltimore, MD 21205, USA.

² Department of Cell Biology, Center for Cell Dynamics, Johns Hopkins University School of Medicine, Baltimore, MD 21205. USA.

³ Institute for Medical Engineering & Science, Department of Biological Engineering, Massachusetts Institute of Technology (MIT), Cambridge, MA 02139, USA.

⁴ Infectious Disease and Microbiome Program, Broad Institute of MIT and Harvard, Cambridge, MA 02139, USA.

⁵ Department of Chemical and Biomolecular Engineering, Johns Hopkins University, Baltimore, MD 21218, USA.

⁶ Roy J. Carver Department of Biochemistry, Biophysics and Molecular Biology, Iowa State University, Ames, IA 50011, USA

⁷ Department of Electrical and Computer Engineering, Whiting School of Engineering, Johns Hopkins University, Baltimore, MD 21218, USA.

^{*} Corresponding authors: srazavi@mit.edu and jctinoue@jhmi.edu

Abstract

Non-linear biomolecular interactions on the membranes drive membrane remodeling that underlies fundamental biological processes including chemotaxis, cytokinesis, and endocytosis. The multitude of biomolecules, the redundancy in their interactions, and the importance of spatiotemporal context in membrane organization hampers understanding the physical principles governing membrane mechanics. A minimal, in vitro system that models the functional interactions between molecular signaling and membrane remodeling, while remaining faithful to cellular physiology and geometry is powerful yet remains unachieved. Here, inspired by the biophysical processes underpinning chemotaxis, we reconstituted externally-controlled actin polymerization inside giant unilamellar vesicles, guiding self-organization on the membrane. We show that applying undirected external chemical inputs to this system results in directed actin polymerization and membrane deformation that are uncorrelated with upstream biochemical cues, indicating symmetry breaking. A biophysical model of the dynamics and mechanics of both actin polymerization and membrane shape suggests that inhomogeneous distributions of actin generate membrane shape deformations in a non-linear fashion, a prediction consistent with experimental measurements and subsequent local perturbations. The active protocellular system demonstrates the interplay between actin dynamics and membrane shape in a symmetry breaking context that is relevant to chemotaxis and a suite of other biological processes.

Keywords Symmetry breaking, giant unilamellar vesicle (GUV), in vitro actin polymerization, cell-mimetic systems, biochemical reconstitution, chemotaxis, spatiotemporal signaling regulation, chemically inducible dimerization (CID), and synthetic biology.

Introduction

Symmetry spans physics and biology. In physics, symmetry was first used to study crystalline structures.¹ As the interplay between form and function has become more well-studied, applications of the concept of symmetry have broadened to other fields of physics and to living biological matter.²⁻⁴ In biology, processes such as chemotaxis, cell division, phagocytosis, and cell-cell fusion are driven by actin polymerization-induced forces that move the plasma membrane in single cells.⁵⁻⁷ Although the direction and magnitude of actin-generated forces can differ depending on the cellular processes at hand, symmetry breaking—a process in which a symmetric system exhibits directed behavior due to a bifurcation—has become a unifying hallmark of these processes.⁸⁻¹¹ Asymmetric arrangement of actin, among other proteins, gives rise to spatial patterns that ultimately regulate cellular differentiation and development.¹²⁻¹⁴ Understanding how actin-induced asymmetries initiate and identifying their implications on function are foundational challenges that remain to be addressed in biophysics.^{3,15,16}

In eukaryotic cells, multiple regulatory mechanisms, including protein switches and allosteric regulation of signal transduction, are known to amplify biomolecular asymmetries. To study actin-induced symmetry breaking, in vitro reconstitution using reduced, membrane-bound systems that lack the biological complexity found in cells have provided insight into the components that regulate actin dynamics. Previous work has shown that cell-sized vesicles, placed in a mixture of actin and its polymerization regulators, experience F-actin-exerted forces on the membrane. These studies found that symmetry was broken in this system only if either capping protein (CP) or myosin were also present. Although they have been informative, these experiments have been limited to cases where actin and its regulators were external to the vesicles and in effectively infinite supply. Further, work with encapsulated molecules have underscored the potential for cell-mimetic approaches that regulate reactions in space and time, inspiring the opportunities to perturb self-organization in a confinement 22,33.

Here, we developed a synthetic platform for the programmable and chemically-inducible control of actin polymerization in giant unilamellar vesicles (GUVs). Using chemical protein dimerization modules as both sensing and actuation units, we show that rapamycin-induced recruitment of an engineered form of ActA, a potent Arp2/3-dependent actin nucleation promoting factor, to the inner leaflet of GUVs activates Arp2/3 complexes, leading to polymerization of G- and F-actin and generation of force on the membrane. We find that our platform couples biochemical cues to actin polymerization and exhibits chemically-induced symmetry breaking, wherein actin polymerization and GUV membrane deformations become asymmetric. Strikingly, when rapamycin is administered globally without a directional preference, the resulting asymmetric actin distributions and membrane deformations are uncorrelated with ActA distributions across GUVs, indicating symmetry breaking. Further microscopic analyses indicate that actin polymerization on the inner leaflets of GUVs results in membrane deformations that impart substantial shape eccentricity to GUVs. Modeling the dynamics of actin polymerization in GUVs, we find that the coupling of actin polymerization to asymmetrically-initiated actin nucleation sites is consistent with the empirically observed spread of actin. Thin-shell modeling further suggests that observations of GUV shape eccentricity are qualitatively consistent with the mechanical deformations imparted by an internal osmotic pressure. with the eccentricity determined by the degree of actin asymmetry. Together, these results demonstrate a synthetic biology platform and mechanistic model for the control of actin polymerization in GUVs, illustrating a tunable approach to the study of symmetry-breaking in self-organization and elucidating the interplay between biological signaling, actin dynamics, and thin-shell mechanics for shape generation.³⁴

Results

Integrating sensing modules inside GUV protocells To develop a synthetic biology-based platform that allows for control of actin polymerization and membrane remodeling in protocells in response to external chemical cues, we designed a protein dimerization-based sensing and actuation module inside GUVs (Supplementary Figure 1). We employed chemically-inducible dimerization (CID) based on FK506 binding proteins (FKBP) and FKBP-rapamycin binding domain (FRB) proteins, which heterodimerize in the presence of a small molecule derived from rapamycin. CID has been predominantly used in cells to manipulate biochemical reactions on the surface of membranes, tether artificial membranes, and mediate phase separation in emulsion, but to our knowledge has not been implemented inside GUVs.

We first individually linked FRB and FKBP to cyan and yellow fluorescent proteins, respectively (6xHis-CFP-FRB and 6xHis-YFP-FKBP). We encapsulated 3.2 µM each of purified forms of these proteins inside GUVs composed of egg-

derived phosphatidylcholine lipid membranes (see Supplementary Table 1 for additional details) generated using the inverted emulsion technique (methods).^{38–41} We found that stimulating the GUVs with an external, undirected supply of rapamycin resulted in heterodimerization of the FKBP and FRB proteins, as indicated by Förster resonance energy transfer (FRET) measurements of CFP. Heterodimerization induced by rapamycin was detected within minutes, showing a more robust performance at 100 µM rapamycin compared to lower concentrations (Supplementary Figure 1), consistent with the concentration range previously reported for in vitro studies^{42,43}. In contrast, administration of vehicle (dimethyl sulfoxide, DMSO) did not result in FRET signal intensity increase, indicating no heterodimerization (Supplementary Figure 1). Our observations verified that our engineered CID modules enable externally-driven signal processing inside GUVs.

To allow for membrane-localized output, we next designed CID-based constructs targeted to GUV membranes. We aimed to concentrate the luminal CFP-FRB at the inner membrane where FKBP was bound in a rapamycin-inducible manner (**Fig. 1A**). To this end, we coupled FKBP to the effector domains of the myristoylated alanine-rich kinase substrate (MARCKS-ED), a positively-charged peptide that binds to phosphatidylserine (PS). The resulting construct, mCherry-FKBP-MARCKS, and luminal CFP-FRB were purified, introduced into PS-containing GUVs (Supplementary Table 1), as we verified MARCKS exhibited no affinity for PC lipids (Supplementary Figure 2). With this design we destined mCherry-FKBP-MARCKS at the membrane while retaining the luminal distribution of FRB (**Fig. 1B**). Upon rapamycin administration, the luminal CFP-FRB localized to membranes (**Fig. 1B,C** and movie S1) within minutes, a timescale similar to that previously observed with CID in mammalian cells. The minute-scale temporal dynamics of our GUV-encapsulated CID system suggests that it can recapitulate actin's temporal dynamics in natural cellular environments.

Inducible, on-demand actin polymerization inside GUVs We next coupled our CID-based constructs targeted to GUV membranes with actin polymerization. We linked FRB to a re-engineered domain of actin assembly-inducing protein, ActA (1-183) (Supplementary Figure 3). ActA is a potent Arp2/3-dependent actin nucleation promoting factor^{46,47} that we recently engineered to generate forces on the cytoplasmic membranes of mammalian cells.⁴⁸ As the purified ActA exhibited nonspecific affinity for PS lipids, for FKBP anchoring to the membrane, we opted for a histidine-nickel affinity approach instead of relying on electrostatic interactions. We encapsulated a purified, C-terminal 2xstrep affinity-tagged form of the ActA-FRB construct, 2xstrep-ActA-FRB-CFP, together with purified Arp2/3 complex, purified G-actin mixed with 8% Alexa Fluor 488-labeled G-actin for visualization, purified 6xHis-tagged mCherry-FKBP, and ATP in GUVs containing nickel-conjugated lipids to enable His-tagged FKBP anchoring and PEG-PE to reduce unspecific protein-membrane interaction (**Fig. 2A, B**, Table 1).

With this design, initially all components, except for membrane-bound mCherry-FKBP, were inside the luminal body. After administration of rapamycin to the external milieu, we found that the engineered ActA redistributed itself on the membrane and activated the Arp2/3 complex, as supported by actin assembly measurements in test tubes (Supplementary Figure 4). Subsequently, stochastic and asymmetric patches of actin emerged on the membrane and grew to engulf the GUV boundary (Fig. 2B and movie S2). With sufficiently high concentrations of G-actin (~3 µM), actin polymerization on the membrane deformed GUVs smaller than ~50 microns in diameter (Fig. 2B). To validate that membrane deformations emerge as a result of actin assembly, we externally administered latrunculin A, a toxin that depolymerizes F-actin, binds G-actin, and hinders actin assembly. ⁴⁹ With latrunculin A present in the media, we found that actin patches failed to grow; additionally, the fluorescence intensities of already-developed F-actin patches decreased over time (Supplementary Figure 5). These results indicate that actin growth was caused by actin polymerization, rather than the accumulation of monomeric G-actin. Indeed, without ActA or Arp2/3, actin failed to polymerize. In the absence of rapamycin, we found that only a baseline level of background luminal actin polymerization occurred (Fig. 2C and Supplementary Figure 6). These observations suggest that a threshold concentration of ActA drives actin polymerization, a finding similar to previous results indicating that the WASP family of Arp2/3 activators⁵⁰ also exhibits a concentration threshold for downstream Arp2/3 activation. Notably, our rapamycin-inducible control of a threshold-dependent signaling cascade, which leads to actin polymerization, provides a system that can explore biological symmetry breaking using only a small number of regulators.

Actin polymerization is dynamic and exhibits symmetry breaking In order to quantify the dynamics of actin polymerization in our model system, we generated kymographs for the spatial distributions of ActA and actin fluorescence intensities, as well as membrane curvature, as functions of time (methods and supplementary materials) (**Fig. 3A**). These kymographs showed that, in typical GUVs, ActA and actin were homogeneously distributed in space until a timescale of \sim 5 min after rapamycin administration (at t=0), after which discrete actin nucleation sites formed

over the membrane surfaces. The resulting actin polymerization generated forces that caused the contraction of the membrane, evident through the heightened intensity of the membrane marker (**Fig. 3A**). Principal component analyses further showed that multiple discrete peaks in the actin and local curvature kymographs, and to a substantially lesser extent in the ActA kymographs, accounted for most of the empirically observed variation across GUVs (Supplementary Figure 7). To investigate whether the heterogeneity of actin nucleation was associated with upstream ActA distribution, we calculated ActA-actin correlations for each of 18 GUVs across time (**Fig. 3B**). These analyses indicated a small ActA-actin correlation of \sim 0.2, which likely arose from lipid artifacts in the membrane where proteins appeared enriched. Importantly, these correlations remained unchanged after the addition of rapamycin. However, discrete and asymmetric actin nucleation occurred after rapamycin addition, as supported by plots of actin fluorescence intensity along the GUV contours (**Fig. 3C**). The absence of correlation increase with respect to ActA therefore indicates that the symmetry breaking is spontaneous and does not depend on detectable levels of ActA, a finding consistent with observations of symmetry breaking in previous studies. 51

We next performed similar correlation analyses for membrane curvature (**Fig. 3B**). These analyses indicated that ActA and actin were essentially uncorrelated with membrane curvature, despite a small increase in correlation from -0.2 to 0 after rapamycin addition for ActA and curvature (**Fig. 3B**). While actin polymerization may lead to local membrane deformations, it is possible that these deformations may manifest in membrane curvature alterations on a global scale. To investigate this hypothesis further, we quantified the entropy as a global measure of variation—reflecting changes in the distributions of values, such that higher entropy values indicate higher asymmetry—across all points on the GUV contours (**Figs. 3C, D**). We calculated the entropy for ActA intensity and actin intensity; additionally, we calculated the eccentricity of the best-fitting ellipse to each GUV contour as a global measure of shape eccentricity. We found that, in contrast to ActA entropy, the actin entropy and eccentricity persistently increased after rapamycin addition. These results are consistent with our observations that actin nucleation is asymmetric and uncorrelated with ActA (**Figs. 3B, D**), and further suggest that asymmetry in the actin distribution is associated with global, but not local, GUV shape changes.

While we have focused on the correlations between ActA, actin, and curvature for each GUV, these correlations may differ globally across GUVs. To investigate this possibility, we computed ActA and actin mean intensity profiles at representative timepoints pre- and post-rapamycin treatment (**Fig. 3E**). Intriguingly, and similar to our previous analyses (**Fig. 3B**), we found no correlation between the mean intensities of ActA and actin after rapamycin treatment, despite the two quantities being moderately positively correlated—possibly due to initial lipid artifacts in the membranes—before rapamycin treatment. Correlations between mean ActA intensity and eccentricity were weaker, while mean actin intensity was uncorrelated with eccentricity before rapamycin treatment. The strongest correlation, of \sim 0.55, emerged between mean actin intensity and eccentricity after rapamycin treatment, again indicating that increased actin polymerization is associated with asymmetric GUV shapes. Taken together, these results further highlight symmetry breaking in actin polymerization and GUV shape in our synthetic platform.

Actin polymerization is associated with GUV shrinkage and shape eccentricity
As our analyses indicate that asymmetric actin polymerization is associated with changes in GUV shape, we further investigated the dynamical and mechanical implications of actin symmetry breaking. Building on our observations of actin fluorescence at the GUV surface across all timepoints, we assumed that a spherical, linear-elastic, and isotropic thin-shell layer of actin is initially anchored to the inner leaflet of each GUV, and that the membrane surface area is larger than that of the actin shell's. The osmolarity of the inner solution was determined to be 1633 mOsmol/kg, while that of the outer solution was 1298 mOsmol/kg (methods). As internal, outward turgor pressure on the order of \sim 0.1 to 1 atm can be generated by the millimolar-scale osmotic imbalance of solutes across the GUV (Table 1), this actin shell is the main load-bearing element, and will be remodeled by additional actin polymerization (**Fig. 4A**).

Previous studies have assumed that the actin polymerization rate outside a droplet, with actin polymerization occurring in one direction, depends on the normal stress in the droplet with a Kramer's rate dependence. Here, building on this assumption of mechanical stress-dependent actin polymerization, we assume that the local, volumetric rate of actin polymerization (dV/dt) at any surface coordinate (θ,φ) and at time t depends on the in-plane mechanical stress, $\sigma(\theta,\varphi,t)$, also as a Kramer's rate: $dV(\theta,\varphi,t)/dt=\ell^3v_0e^{\sigma(\theta,\varphi,t)/\sigma_0}$, where σ_0 is a baseline value of stress, ℓ is the length of an actin monomer, and v_0 is a unit rate of actin polymerization. For a spherical actin shell, the nonvanishing in-plane stresses are $\sigma_0=pr_0/2h_0$, where p is the turgor pressure, r_0 is the shell radius, and h_0 is the initial actin shell thickness. Anticipating that ActA-dependent actin polymerization results in the local shell thickness being multipled by a factor of $f\gg 1$, we expect that the ActA-enriched regions with highest mechanical stress are at the leading edges;

this is confirmed by finite-element simulations of pressurized spherical shells with two different thicknesses (**Fig. 4B** and Supplementary Information). When actin finishes polymerizing laterally across the GUV surface at time t', the stresses are approximately homogeneous and the form of dV/dt suggests that actin thickens linearly in time. Detailed calculations for this model (Supplementary Information) predict that:

$$c(t) \sim \cos^{-1}\left(1 - \frac{\ell^2 v_0 e^f t}{r_0^2}\right) \ (t < t'), \quad h(t) \sim t \ (t \ge t'), \quad r(t) \sim 1/t \ (t \ge t'), \tag{1}$$

where c(t) is the fraction of the shell circumference at which ActA-dependent actin polymerization has already occurred at time t, h is the polymerized thickness of the actin shell at time t, and r is the radius of the actin shell at time t, which decreases due to shell thickening counteracting the turgor pressure and decreasing the mechanical strain, ε , in the actin shell (supplementary information). For characteristic values of all other parameters, fitting the unit actin polymerization rate (v_0) predicts both the quantitative rates of actin's lateral expansion and thickening, and we find that these rates and the resulting shrinkage of the actin shell are consistent with our empirical observations (Fig. 4C). Furthermore, quantifying the magnitude of GUV shrinkage toward the end of our timelapses reveals a radial shrinkage on the order of $\sim 5\%$, consistent with our model predictions (Fig. 4C).

The consistency between our empirical observations and our biophysical model therefore suggests that asymmetric actin polymerization is a dynamical process that results in mechanical alterations to GUVs. Moreover, at long timescales, actin thickening can result in GUV actuation. Given that actin symmetry breaking was also associated with shape eccentricity (**Fig. 3D**), we further investigated whether mechanical deformations could give rise to substantial shape eccentricity. For simplicity, we modeled actin as a shell with two thicknesses, using finite-element simulations across a range of angles subtended by the thicker actin (**Fig. 4D**). We found that, for finite values of mechanical strain and across a broad range of shell thicknesses, the shape of the simulated actin shell was eccentric and could be fit by ellipsoids with eccentricity values on the order of \sim 0.2 (**Fig. 4D**), consistent with the magnitude of eccentricity values inferred from experiments (**Fig. 3D**). These results indicate that shape asymmetry can arise as a mechanical consequence of actin symmetry breaking alone.

Asymmetric inputs validate time-scales and elucidate the origins of symmetry breaking In order to further probe our system, we reduced its spatial degrees of freedom by constraining the position of the rapamycin input. We induced a rapamycin gradient on the length-scale of a GUV using a point source by administering ethanol-solubilized rapamycin with a microinjector close to each GUV and adding Alexa Fluor 647 dye to track the rapamycin gradient (as its Stokes radius is comparable to that of rapamycin⁵³). Initial experiments with POPC lipids highlighted fast actin spreading around the GUV hampering a local response (Supplementary Figure 8). In order to confine the localization further, we used deformable DPPC lipids, which exhibit lower lateral diffusion and membrane fluidity as compared to POPC lipids and yet still deform upon actin polymerization⁵⁴ (Supplementary Figure 9 and Supplementary Table 1). Additionally, with all other conditions held constant, we reduced the ActA concentration to limit its availability (Fig. 5A and Supplementary Table 2). After administering rapamycin locally, we observed that ActA always translocated towards the membrane region proximal to the needle tip, and within ∼5 minutes, ActA decorated the entire GUV membrane. Furthermore, we found that subtle, but stable, ActA localization at the needle tip, on the order of ~1 minute, was sufficient to bias an actin nucleation site to appear at the same site. These observations are consistent with the actin nucleation dynamics observed in an in vitro pyrene assay (Supplementary Figure 4). Intriguingly, transient ActA leading to stable actin accumulation is reminiscent of memory behavior due to time delay,55 and these observations indicate that ActA may store positional information downstream of the local amplification potentially mediated by the Arp2/3 complex (Supplementary Figure 10).

Downstream of transient ActA localization, we found that, within \sim 15 minutes—by which time the ActA distribution appeared uniform across the membrane—F-actin patches emerged next to the needle tip and grew to encompass \sim 85% of the membrane (**Fig. 5B, C**, and movie S3), expanding laterally and in thickness similarly to our previous experiments, in which rapamycin was administered without a directional bias. These results show that asymmetric actin polymerization is uncorrelated with ActA irrespective of the route (undirected or directed) of rapamycin induction. As in the previous experiments, substantial shape eccentricity and membrane shrinkage also occurred, consistent with our model predictions (**Fig. 4D**). Additional perturbations support that actin symmetry breaking is associated with local fluctuations in rapamycin concentration, and that actin polymerization is indeed required for membrane shape deformations: when we altered the needle placement in independent experiments, we observed a positive correlation between the needle tip and actin polymerization initiation sites. This manipulation ruled out the possibility of flow-based interference or phase-separated lipids driving the local output (**Figs. 5C, D** and Supplementary Figure 10), and further suggested that

local, non-equilibrium fluctuations in rapamycin concentration—which may result in small ActA fluctuations not seen in our correlation analyses—is associated with actin symmetry breaking **Fig. 5E**. Consistent with this hypothesis, we found enhanced localization of F-actin after increasing the GUV diameter size, suggesting that symmetry breaking is length-scale dependent (**Figs. 5B, C, D** and Supplementary Figures 11 and 13). To determine the radial rate of actin polymerization, we analyzed the slope of the actin kymographs (Supplementary Figure 14 and methods). Our observations revealed that the polymerization rate correlates with the size of the GUVs, occurring more rapidly in smaller ones. Additionally, the distinction between local and global input influences the number of actin peaks that emerge. For larger GUVs, the relatively large membrane surface adjacent to the needle likely depletes the reaction substrate and serves as an internal non-molecular inhibitory element.

We last investigated the factors influencing actin thickening and GUV shape deformations (**Fig. 5D**). To assess if we can sculpt this thickening by integrating additional actin modulators, we used a purified capping protein, Cap32/34, which binds the barbed end of actin, preventing actin monomer addition or loss. In the presence of $100\ nM$ of purified Cap32/34, ⁵⁶ we found that actin patches became sparse and thin and eventually disintegrated. This indicated that actin polymerization at barbed ends underlied actin thickening, consistent with bulk actin polymerization assay measurements (Supplementary Figure 4) in which actin polymerization was inhibited with overloaded Cap32/34 ($3\ \mu M$; Supplementary Figure 12). Moreover, addition of cofilin, which promotes actin disassembly in conjunction with Cap32/34, abolished actin thickening in response to local administration of rapamycin. With Cap32/34 at a relatively low concentration ($50\ nM$), we did not observe membrane protrusion or invagination even in the presence of higher concentrations of G-actin (Supplementary Figure 12), suggesting that shape deformations were bottlenecked by actin polymerization. Taken together, these results suggest that the timescale of ActA stability is critical to achieving a stable actin polymerization output, and that actin polymerization is needed for shape deformations. Additionally, these experiments further suggest that symmetry breaking is associated with local fluctuations in rapamycin concentration.

Discussion

In vitro cell mimetic systems aim to assemble the minimal set of protein and lipid modules to output a desired function. Here, we have developed a cell mimetic platform that implements spatiotemporal control modules to achieve biological symmetry breaking with actin. To our knowledge, our platform comprises the most reduced network of biological nodes that is able to produce symmetry breaking in a context relevant to diverse physiological processes, including chemotaxis. Specifically, our design is devoid of capping protein, myosin, or phase-separated lipids that were previously considered indispensable to symmetry breaking. Using our synthetic platform, we have found that the application of undirected external chemical inputs results in directed actin polymerization and asymmetric membrane deformations. The actin polymerization and shape deformations are uncorrelated with upstream biochemical cues, indicating biological symmetry breaking. Biophysical modeling suggests that a model of actin polymerization is consistent with our experimental observations and can lead to substantive membrane shape changes through mechanical deformations. Local experiments, in which rapamycin is directionally administered, further confirm these dynamics and suggest that actin symmetry breaking arises from local fluctuations in rapamycin concentration.

Our work therefore shows that signal amplification from upstream chemical components, including Arp2/3, to actin is sufficient to drive symmetry breaking. Moreover, our platform exemplifies how implementing CID in an active model system can lead to changes in the system's mechanical and morphological properties. We observed that seconds-long local ActA enrichment on the membrane close to the input was sufficient to bias the F-actin towards the input source, a finding which points to the potential positive feedback characteristic of actin polymerization in response to ActA-induced Arp2/3 activation⁵⁹ and which could be further interrogated with Arp2/3 mutant variants for more fine-tuned control of symmetry breaking. While challenging, but obtaining higher-resolution structural information of the Arp2/3 and actin molecules inside GUVs could guide mechanisms of activation in a membrane context⁶⁰.

Our biophysical modeling of the dynamics and mechanics of actin polymerization underscores the interplay between actin symmetry-breaking and GUV shape deformations. Other models have been developed to describe actin dynamics and mechanics in other contexts; notably, these models have focused on different aspects of actin polymerization, including actin flow²⁵ and settings of reduced dimensionality.⁵² The model developed in this work is specific to our platform in that it focuses on the patterns of actin polymerization generated through CID, as well as the stretching deformations caused by an internal osmotic pressure. Our model suggests that the mechanical stress-dependent incorporation of actin subunits at actin nucleation sites is consistent with our empirical observations, and that the coupling of asymmetric actin patterning with thin-shell mechanical properties alone can generate asymmetric GUV shapes. Our model and its

conclusions may generalize beyond our experimental platform to offer physical insights into other processes, including actin-dependent cell shape changes and cell motility.

In general, bottom-up approaches that rely on de novo assembly to understand biophysical principles have recently gained traction in synthetic biology. Our work exemplifies these efforts on the molecular scale. The presented platform provides insight on the spatiotemporal localization of the molecular components and elucidates the design principles governing chemical signaling, actin assembly, and symmetry breaking. Our platform offers a novel GUV manipulation technique^{61,62} and a versatile imaging pipeline to track the locality-specific concentration of biomolecules in a dynamic GUV over time, complementing other realized modalities. ^{63,64} Our developed image processing and statistical analysis scheme enables probing the biomolecular and geometric features of symmetry breaking, a pipeline that is is applicable to other GUV- and cell-based studies. By combining experiment and modeling, our results offer the ability to better understand macroscopic cellular processes, including morphogenesis, motility, and division, that build on fundamental biophysical and active matter principles to accomplish complex biological tasks.

Methods

DNA plasmid construction and protein purification Detailed in Supplementary Materials.

GUV fabrication GUVs were prepared adopting our previously reported protocol. ^{39,40} Lipids were purchased from Avanti in their chloroform-solubized form and were aliquoted with a glass pasteur pipette to achieve the desired final molar concentrations. The lipids underwent vacuum drying overnight. Except for Egg-PC lipids, which were dissolved in mineral oil, all other lipids were dissolved in hexadecane at a concentration of 1 mg/ml in a Hybaid HS9320 rotisserie hybridization oven, maintaining a temperature of at least 65 $^{\circ}$ C, depending on the lipid's transition temperature. To assemble the GUVs, 300 μ L of the outer GUV solution was placed in a test tube, and 300 μ L of the room temperature lipid mixture containing the outer leaflet was gently pipetted on top. The two layers were left undisturbed for 10-15 minutes. The inner leaflet lipid mix, identical to the outer leaflet in our case, was combined with 100 μ L of the droplet containing the desired GUV content. This mixture was vigorously tapped to achieve a homogenous turbid emulsion phase, which was then gently pipetted into the test tube to form the third layer. Following centrifugation at 2,500g for 7 minutes, the bottom of the tube was punctured with a needle to collect the bottom-most layer containing GUVs floating in the outer solution. The osmolarities of the inner and outer GUV buffer were measured with a Gonotec® Osmomat 3000TM.

Global CID-based protein translocation in GUVs For CFP-FRB translocation towards the mCherry-FKBP-MARCKS-bound membrane, we reconstituted 4.4 μM FRB-containing and 7.8 μM FKBP-containing constructs in PBS buffer inside symmetric GUVs (Supplementary Table 1) using the inverted emulsion-based GUV fabrication technique previously reported. To balance the osmotic pressure, 750 mM sucrose was reconstituted inside while the GUVs were collected in 750 mM glucose containing PBS buffer. 100 μ M DMSO-solubilized rapamycin was administered in the outer GUV buffer to trigger translocation. For actin polymerization experiments we reconstituted the components reported in Table 1.

Global rapamycin administration image acquisition For CFP-FRB translocation experiments, we used an inverted epi-fluorescence microscope (Axiovert135TV, ZEISS) with 40× oil objective to track the CFP and mCherry signal intensity at one frame per 60 seconds. For actin polymerization experiments we used LSM780 confocal microscope (Zeiss) equipped with Plan-Aprochromat 63X/1.40 N.A. oil immersion DIC objective lens (Zeiss 420782-9900).

Image processing and biophysical parameters extraction For Figure 1 and Supplementary Figure 1 Meta-Morph® software (Molecular Devices) was used to measure the average luminal and membrane fluorescence intensity for either CFP or mCherry. Values are reported after normalizing by the average intensities of each prior to rapamycin or DMSO treatment. All actin-containing microscopy data was analyzed using a custom MATLAB® (MathWorks) script (Supplementary Material and code). For pre-processing, image sequences were regionally cropped and smoothed with 2D median and Gaussian filtering. Individual GUVs were segmented based on membrane marker signal (mCherry-FKBP-MARCKs) using intensity thresholding, morphological operations, and active contours technique.

Local rapamycin administration with a microinjector and image acquisition
The GUV content is listed in Supplementary Table 2. A 100 µL droplet of freshly prepared GUVs was placed in a 1-well Lab-Tek II chambered cover glass (Thermo Scientific) immediately before imaging. Local stimulation of GUVs was carried out by lowering a micropipette (Femtotips, Eppendorf) loaded with 10 µL of a freshly prepared solution of 500 µM rapamycin and 100 µM AlexaFluor 647 dye (Thermo Scientific) and applying microinjection near GUVs of interest. The rapamycin-dye solution was rapidly prepared on ice in a 100 µL volume, diluted in double distilled H₂O from stock solutions of rapamycin (5mM in 100% ethanol) and AlexaFluor 647 (1 mM in DMSO). Concentrations were optimized based on estimates of micropipette-generated chemical gradients under passive diffusion or forced flow⁶⁵ and considerations of needle clogging. The micropipette was then connected to a microinjector (Femtojet, Eppendorf) controlled by a micromanipulator (Eppendorf). Image acquisition began with the micropipette immersed in the liquid droplet but above the focal plane of GUVs, at an initial compensation pressure (P_c) of 5-10 hPa. To achieve local chemical dimerization, the micropipette was lowered near a GUV in the field of view, and compensation pressure was increased to between 30 - 50 hPa for a continuous local gradient. To relieve clogging and generate brief local gradients, microinjection pressures were also applied in bursts as needed (injection parameters: injection pressure (P_i) = 400 - 800 hPa; injection duration (t_i) = 5-10 sec; P_c = 10 hPa). Confocal image acquisition every 15 seconds was performed on LSM780 confocal laser-scanning microscope (Zeiss).

Reagents Rabbit skeletal muscle actin (AKL99), pyrene-labeled actin (AP05), Arp2/3 complex (RP01P), and GST-WASP-VCA (VCG03-A) were purchased from Cytoskeleton. ATP for actin dialysis buffer was purchased from Gold Biotechnology. All lipids (Supplementary Table 1) were purchased from Avanti Polar Lipids. Hexadecane (H6703) and silicone oil (viscosity 20 cSt (25 °C), 378348) were purchased from Sigma Aldrich.

Statistical Analysis Symmetry breaking analysis from kymographs using correlation analysis, and principal component analysis are detailed in Supplementary Materials. To verify our method, we applied our analysis pipeline to a previously reported case of symmetry breaking in GUVs (Supplementary Figure 15).⁵¹ Please refer to the figure legends for the description of sample size and the corresponding statistical methods used.

Supplementary Materials Included in a separate PDF file.

References and Notes

- ¹ DJ Gross, The role of symmetry in fundamental physics. *Proceedings of the National Academy of Sciences of the United States of America* **93**, 14256–14259 (1996).
- ² S Katzir, The emergence of the principle of symmetry in physics. *Historical Studies in the Physical and Biological Sciences* **35**, 35–65 (2004).
- ³ R Li, B Bowerman, Symmetry Breaking in Biology. Cold Spring Harbor Perspectives in Biology **2(3)**, a003475 (2010).
- ⁴ S Razavi, T Inoue, Reconstitution of membrane symmetry breaking in *Plasma Membrane Shaping*. (Elsevier), pp. 333–353 (2022).
- ⁵ TD Pollard, JA Cooper, Actin, a central player in cell shape and movement (2009).
- ⁶ K Shilagardi, et al., Actin-propelled invasive membrane protrusions promote fusogenic protein engagement during cell-cell fusion. *Science* **340** (**6130**), 359–363 (2013).
- ⁷ PN Devreotes, et al., Excitable Signal Transduction Networks in Directed Cell Migration. *Annual Review of Cell and Developmental Biology* **33**, 103–125 (2017).
- ⁸ T Svitkina, The actin cytoskeleton and actin-based motility. *Cold Spring Harbor Perspectives in Biology* **2;10(1)**, a018267 (2018).
- ⁹ N Johnson, et al., Actin-filled nuclear invaginations indicate degree of cell de-differentiation. *Differentiation* **71**, 414–424 (2003).
- ¹⁰ C Le Clainche, MF Carlier, Regulation of actin assembly associated with protrusion and adhesion in cell migration. *Physiological Reviews* **88**, 489–513 (2008).
- ¹¹ AE Carlsson, Membrane Bending by Actin Polymerization. *Current Opinions Cell Biology* **50**, 1–7 (2018).
- ¹²S Sawai, Y Maeda, Y Sawada, Spontaneous symmetry breaking Turing-type pattern formation in a confined Dictyostelium cell mass. *Physical Review Letters* (2000).
- ¹³ SM Sears, M Soljačić, DN Christodoulides, M Segev, Pattern formation via symmetry breaking in nonlinear weakly correlated systems. *Physical Review E Statistical Physics, Plasmas, Fluids, and Related Interdisciplinary Topics* (2002).
- ¹⁴ I Salazar-Ciudad, J Jernvall, SA Newman, Mechanisms of pattern formation in development and evolution. *Development* **130**, 2027–2037 (2003).
- ¹⁵ J van der Gucht, C Sykes, A Physical Model of Cellular Symmetry Breaking in *Biological Physics: Poincaré Seminar* 2009, ed. V Rivasseau. (Springer Basel, Basel), pp. 33–46 (2011).
- ¹⁶ NH Wubshet, B Wu, S Veerapaneni, AP Liu, Differential regulation of GUV mechanics via actin network architectures. *Biophysical Journal* (2022).
- ¹⁷ AB Goryachev, M Leda, W Bement, Many roads to symmetry breaking: Molecular mechanisms and theoretical models of yeast cell polarity (2017).
- ¹⁸ R Nussinov, CJ Tsai, H Jang, Are Parallel Proliferation Pathways Redundant? (2020).
- ¹⁹ LL Pontani, et al., Reconstitution of an actin cortex inside a liposome. *Biophysical Journal* **96**, 192–198 (2009).
- ²⁰ KR Levental, I Levental, Chapter Two Giant Plasma Membrane Vesicles: Models for Understanding Membrane Organization in *Current Topics in Membranes*, ed. AK Kenworthy. (Academic Press) Vol. 75, pp. 25–57 (2015).
- ²¹ M Doktorova, et al., Preparation of asymmetric phospholipid vesicles for use as cell membrane models. *Nature Protocols* **13**, 2086–2101 (2018).
- ²² J Lemière, K Carvalho, C Sykes, Cell-sized liposomes that mimic cell motility and the cell cortex. *Methods in Cell Biology* **128**, 271–285 (2015).
- ²³ AP Liu, et al., Membrane-induced bundling of actinfilaments. *Nature Physics* **4**, 789–793 (2008).
- ²⁴ K Carvalho, et al., Actin polymerization or myosin contraction: Two ways to build up cortical tension for symmetry breaking. *Philosophical Transactions of the Royal Society B: Biological Sciences* **110**, 16456–16461 (2013).
- ²⁵ C Simon, et al., Actin dynamics drive cell-like membrane deformation. *Nature Physics* **15**, 602–609 (2019).
- ²⁶ R Lopes dos Santos, C Campillo, Studying actin-induced cell shape changes using Giant Unilamellar Vesicles and reconstituted actin networks. *Biochemical Society Transactions* **50**, 1527–1539 (2022).
- ²⁷ N Ierushalmi, et al., Centering and symmetry breaking in confined contracting actomyosin networks. *eLife* **9**, e55368 (2020).

- ²⁸ T Litschel, et al., Reconstitution of contractile actomyosin rings in vesicles. *Nature Communications* **12**, 2254 (2021).
- ²⁹ R Sakamoto, et al., Tug-of-war between actomyosin-driven antagonistic forces determines the positioning symmetry in cell-sized confinement. *Nature Communications* **11**, 3063 (2020).
- ³⁰ Y Bashirzadeh, H Moghimianavval, AP Liu, Encapsulated actomyosin patterns drive cell-like membrane shape changes. iScience 25, 104236 (2022).
- ³¹ L Baldauf, et al., Biomimetic actin cortices shape cell-sized lipid vesicles. bioRxiv p. 2023.01.15.524117 (2023).
- ³² NA Araújo, et al., Steering self-organisation through confinement. Soft Matter 19, 1695–1704 (2023).
- ³³ NH Wubshet, AP Liu, Methods to mechanically perturb and characterize GUV-based minimal cell models. *Computational and Structural Biotechnology Journal* **21**, 550–562 (2023).
- ³⁴ J Aguilar, et al., A review on locomotion robophysics: the study of movement at the intersection of robotics, soft matter and dynamical systems. *Reports on progress in physics. Physical Society (Great Britain)* **79**, 110001 (2016).
- ³⁵ R Derose, T Miyamoto, T Inoue, Manipulating signaling at will: chemically-inducible dimerization (CID) techniques resolve problems in cell biology. *Pflugers Archiv: European Journal of Physiology* **465**, 409–417 (2013).
- ³⁶ CB Carbone, et al., In vitro reconstitution of T cell receptor-mediated segregation of the CD45 phosphatase. *Proceedings of the National Academy of Sciences* **114**, E9338–E93458 (2017).
- ³⁷ RM Caldwell, et al., Optochemical Control of Protein Localization and Activity within Cell-like Compartments. *Biochemistry* 57, 2590–2596 (2018).
- ³⁸ S Pautot, BJ Frisken, DA Weitz, Production of Unilamellar Vesicles Using an Inverted Emulsion. *Langmuir* **19**, 2870–2879 (2003).
- ³⁹ EL Meier, S Razavi, T Inoue, ED Goley, A novel membrane anchor for FtsZ is linked to cell wall hydrolysis in Caulobacter crescentus. *Molecular Microbiology* **101**, 265–280 (2016).
- ⁴⁰ S Razavi, T Inoue, T Luo, DN Robinson, Methods for making giant vesicles and their use (2017).
- ⁴¹ Y Zhang, H Obuchi, T Toyota, A Practical Guide to Preparation and Applications of Giant Unilamellar Vesicles Formed via Centrifugation of Water-in-Oil Emulsion Droplets. *Membranes* **13** (2023).
- ⁴² T Inobe, N Nukina, Rapamycin-induced oligomer formation system of FRB-FKBP fusion proteins. *Journal of Bioscience and Bioengineering* **122**, 40–46 (2016).
- ⁴³ H Nakamura, et al., Intracellular production of hydrogels and synthetic RNA granules by multivalent molecular interactions. (2018).
- ⁴⁴ U Dietrich, P Krüger, T Gutberlet, JA Käs, Interaction of the MARCKS peptide with PIP2 in phospholipid monolayers. *Biochimica et Biophysica Acta (BBA) - Biomembranes* **1788**, 1474–1481 (2009).
- ⁴⁵ S Razavi, S Su, T Inoue, Cellular Signaling Circuits Interfaced with Synthetic, Post-Translational, Negating Boolean Logic Devices. *ACS Synthetic Biology* **3**, 676–685 (2014).
- ⁴⁶ TP Loisel, R Boujemaa, D Pantaloni, MF Cartier, Reconstitution of actin-based motility of Listeria and Shigella using pure proteins. *Nature* **401**, 613–616 (1999).
- ⁴⁷ MF Carlier, S Wiesner, C Le Clainche, D Pantaloni, Actin-based motility as a self-organized system: mechanism and reconstitution in vitro. *Comptes Rendus Biologies* **326**. 161–170 (2003).
- ⁴⁸ H Nakamura, et al., ActuAtor, a Listeria-inspired molecular tool for physical manipulation of intracellular organizations through de novo actin polymerization. *Cell reports* **42** (2023).
- ⁴⁹ I Fujiwara, ME Zweifel, N Courtemanche, TD Pollard, Latrunculin A Accelerates Actin Filament Depolymerization in Addition to Sequestering Actin Monomers. *Current Biology* **28**, 3183–3192 (2018).
- ⁵⁰ S Wiesner, et al., A biomimetic motility assay provides insight into the mechanism of actin-based motility. *Journal of Cell Biology* **160**, 387–398 (2003).
- ⁵¹ E Abu Shah, K Keren, Symmetry breaking in reconstituted actin cortices. *eLife* **2014** (2014).
- ⁵² H Boukellal, O Campás, JF Joanny, J Prost, C Sykes, Soft Listeria: Actin-based propulsion of liquid drops. *Physical Review E Statistical Physics, Plasmas, Fluids, and Related Interdisciplinary Topics* 69, 4 (2004).
- ⁵³ B Lin, et al., Synthetic spatially graded Rac activation drives cell polarization and movement. *Proceedings of the National Academy of Sciences* **109**, E3668–E3677 (2012).
- ⁵⁴ D Scherfeld, N Kahya, P Schwille, Lipid Dynamics and Domain Formation in Model Membranes Composed of Ternary Mixtures of Unsaturated and Saturated Phosphatidylcholines and Cholesterol. *Biophysical Journal* 85, 3758–3768 (2003).

- ⁵⁵ A Otto, W Just, G Radons, Nonlinear dynamics of delay systems: An overview (2019).
- ⁵⁶ U Haus, H Hartmann, P Trommler, AA Noegel, M Schleicher, F-Actin capping by cap3234 requires heterodimeric conformation and can be inhibited with PIP2. *Biochemical and Biophysical Research Communications* **181**, 833–839 (1991).
- ⁵⁷ K Dürre, et al., Capping protein-controlled actin polymerization shapes lipid membranes. *Nature Communications* **9**, 1630 (2018).
- ⁵⁸ KY Lee, et al., Photosynthetic artificial organelles sustain and control ATP-dependent reactions in a protocellular system. *Nature Biotechnology* **36**, 530–535 (2018).
- ⁵⁹ AE Carlsson, Growth velocities of branched actin networks. *Biophysical Journal* **84**, 2907–2918 (2003).
- ⁶⁰ B Ding, et al., Structure of Arp2/3 complex at a branched actin filament junction resolved by single-particle cryoelectron microscopy. Proceedings of the National Academy of Sciences of the United States of America 119 (2022).
- ⁶¹ T Toyota, Y Zhang, Identifying and Manipulating Giant Vesicles: Review of Recent Approaches. *Micromachines* **13** (2022).
- ⁶² T Tosaka, K Kamiya, Function Investigations and Applications of Membrane Proteins on Artificial Lipid Membranes. *International Journal of Molecular Sciences* **24** (2023).
- ⁶³ A Caliari, MM Hanczyc, M Imai, J Xu, T Yomo, Quantification of Giant Unilamellar Vesicle Fusion Products by High-Throughput Image Analysis. *International Journal of Molecular Sciences* **24** (2023).
- ⁶⁴ L van Buren, GH Koenderink, C Martinez-Torres, DisGUVery: A Versatile Open-Source Software for High-Throughput Image Analysis of Giant Unilamellar Vesicles. *ACS Synthetic Biology* **12**, 120–135 (2023).
- ⁶⁵ M Postma, PJ van Haastert, Mathematics of experimentally generated chemoattractant gradients in *Methods in Molecular Biology*. Vol. 1407, pp. 381–396 (2016).
- ⁶⁶ TPJ Knowles, MJ Buehler, Nanomechanics of functional and pathological amyloid materials. *Nature Nanotechnology* **6**, 469–479 (2011).
- ⁶⁷ F Gittes, B Mickey, J Nettleton, J Howard, Flexural rigidity of microtubules and actin filaments measured from thermal fluctuations in shape. *Journal of Cell Biology* **120**, 923–934 (1993).
- ⁶⁸ J Zenker, et al., Expanding Actin Rings Zipper the Mouse Embryo for Blastocyst Formation. Cell 173, 776–791 (2018).
- ⁶⁹ R Kusters, et al., Actin shells control buckling and wrinkling of biomembranes. *Soft Matter* **15**, 9647–9653 (2019).

Acknowledgements We extend our gratitude to Dr. Jian Liu and Eduardo Sandoval for their insight on force modeling. We are grateful to Dr. Tianzhi Luo for assistance with vesicle fabrication techniques and Elmer Rho for help with cloning and analyzing FRET data. We thank Dr. Cécile Sykes, Dr. Winston Timp, and Dr. Rong Li for invaluable discussions, Dr. Erin Goley for suggestions and support of the FPLC and fluorimetry experiments, Dr. Daniel Raben for sharing lipid handling setup, and Dr. Koki Kamiya and Dr. Masashi Tabuchi for experimental suggestions on lipid membranes and GUV fabrication. We thank Dr. Masato Kanemaki for the strep-tag plasmids and Robert DeRose for proofreading the manuscript. We are also grateful to Dr. Cristina Martinez-Torres group for generously sharing the beta version of the DisGUVery image analysis pipeline with us.

Data and materials availability All the data associated with this work are presented in the manuscript and its associated supplementary files.

Code availability General MATLAB® code for use in .tif file processing and analysis are available under an open-source license in the GitHub repository https://gitfront.io/r/basharif/gTdvogxUoH4y/GUV-symmetry-breaking-analysis/. Specific .m scripts for each experiment, as well as Abaqus FEA input files used for finite-element simulations, are available from the corresponding authors upon request.

Author contributions S.R. and T.I. conceived the project. S.R. designed and performed the experiments and analyzed data. S.R. implemented the microinjector experiments with help from B.A.-S. F.W. performed modeling. B.A.-S. developed the image processing and statistical analysis pipeline with input from P.I., F.W., and S.R. H.T.M. performed the pyrene assay and purified and labeled actin with help from B.C. H.N. developed and characterized the ActA tool. N.T.H.N performed the osmolarity measurements. P.I. helped with modeling. D.N.R. provided protein purification and GUV fabrication resources. S.R. and F.W. wrote the manuscript with help from T.I., and B.A.-S. All authors contributed to editing of the manuscript.

Funding This work was supported by the National Institute of Health (5R01GM123130, R01GM136858, R35GM149329 to T.I., R35GM128786 to B.C., R01GM149073 to D.N.R. and P.A.I., R01GM66817 to D.N.R., and S10OD016374 to Scot C. Kuo), the DoD DARPA (HR0011-16-C- 0139 to P.A.I., D.N.R. and T.I.), the National Science Foundation (000819255 to T.I., J.L., B.C.), and the PRESTO program of the Japan Science and Technology Agency (PRESTO, JPMJPR12A5 to T.I. and JPMJPR20KA to H.T.M.). S.R. was supported by the National Science Foundation and the Japan Society for the Promotion of Science (JSPS) East Asia and Pacific Summer Institutes and Johns Hopkins Lucille Elizabeth Hay graduate fellowships.

Competing interests S.R., T.I., D.N.R. are inventors on a filed GUV fabrication method patent (US2021/0145746A1).

Main Figures and Table

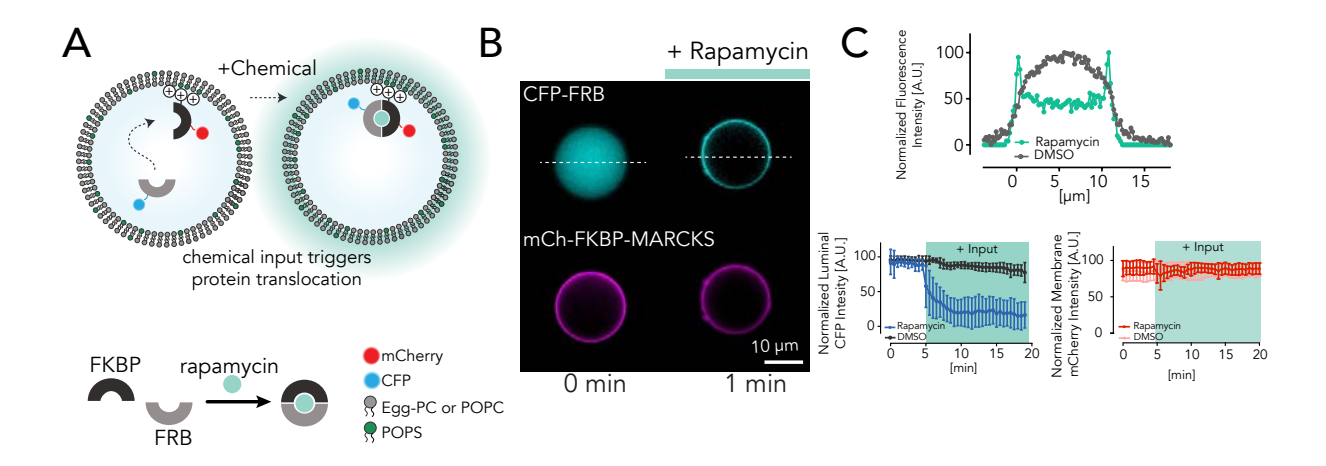


Figure 1. Reconstitution of actuation inside protocells. A. Schematic of the GUVs containing the membrane-anchored mCh-FKBP-MARKCS and luminal CFP-FRB proteins. Rapamycin-induced dimerization of FKBP and FRB moves the CFP-FRB protein towards the membrane. B. Epi-fluorescence images of CFP-FRB (4.4 μM) and mCh-FKBP-MARKCS (7.8 μM) in the symmetric GUVs containing POPC: POPS (4:1 mol%) in the inner lipid leaflet. The initially luminal CFP-FRB protein switches localization to the membrane within minutes post-rapamycin administration. C. Line scans of the mCherry and CFP fluorescence intensity across the vesicle show protein localization before and after rapamycin addition (top). The luminal fluorescence intensity of the CFP-FRB (bottom) normalized by the average of the initial values prior to rapamycin treatment is plotted, highlighting the minute-scale CFP-FRB translocation towards the membrane only in the presence of rapamycin but not DMSO vehicle. The mCherry signal associated with the membrane marker remains membrane-localized throughout the experiment. n=14 for both rapamycin and DMSO conditions. Error bars represent standard deviation. The green box marks rapamycin presence.

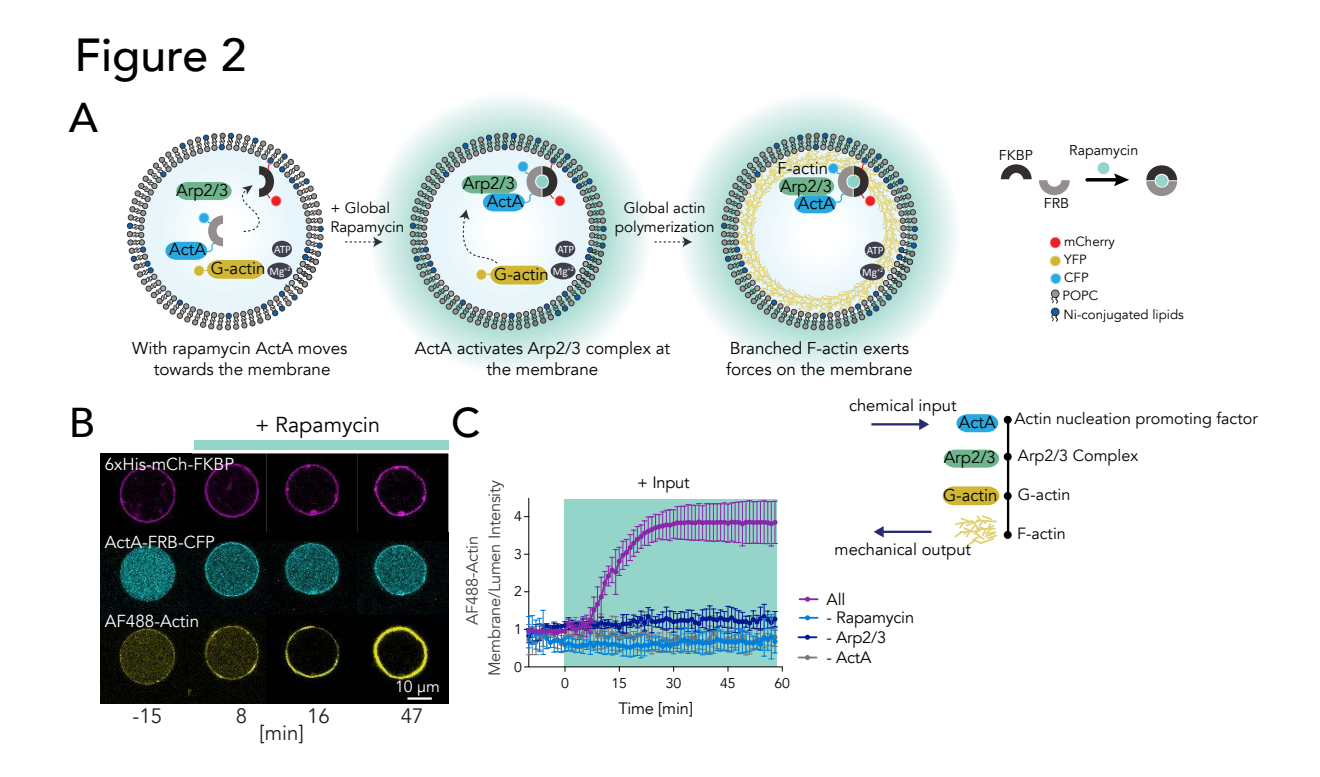


Figure 2. Reconstitution of actin-induced force generation inside rapamycin sensing active protocell. A. Schematic of the signaling pathway. ActA activates Arp2/3 complex on the membrane, where F-actin branches grow to generate force. CID system modules coupled with ActA (1-183) transduce rapamycin sensing to force actuation. ActA (1-183)-FRB-CFP, Arp2/3, and G-actin are initially diffuse in the lumen. mCherry-FKBP is anchored at the membrane. B. Confocal images of symmetric POPC: DGS-NTA(Ni): PEG-PE (95:4:1) GUVs containing 6xHis-mCh-FKBP, ActA (1-183)-FRB-CFP (2 μ M), Arp2/3 (150 nM), G-actin (3 μ M), and ATP (1 mM) in Mg²+ buffer. All protein constructs except 6xHis-mCh-FKBP are luminal at t=0. With rapamycin (10 μ M final concentration), ActA translocates to the membrane and triggers F-actin forces. C. Time-course of mean actin localization in the presence of rapamycin and all components of the signaling cascade, as well as negative controls where Arp2/3, ActA, or rapamycin are absent. n=6 for All, n=4 for -Arp2/3, n=9 for -ActA, and n=10 for DMSO conditions. Error bars indicate standard deviations (SDs). Green area marks rapamycin presence.

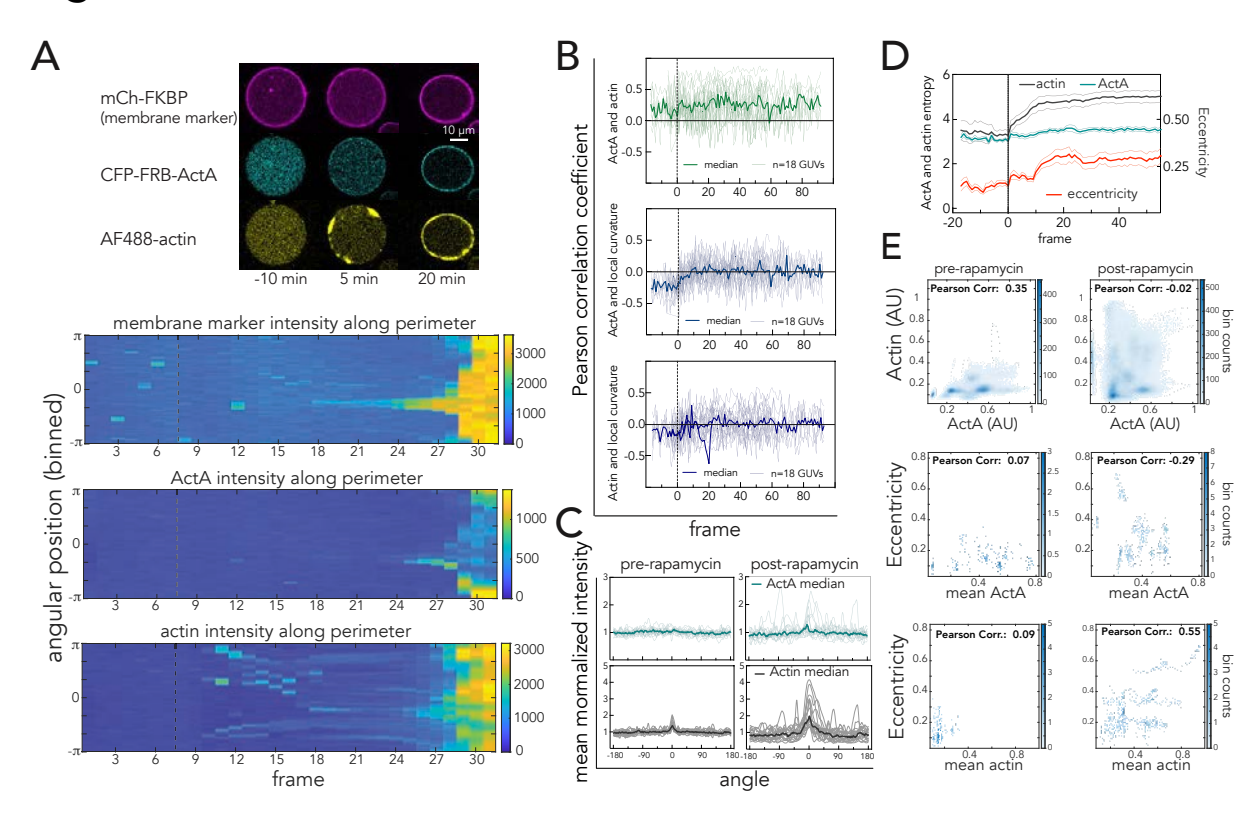


Figure 3. Symmetry breaking in biochemical and physical spaces on a local and global scale. A. Representative confocal image of a GUV before and after rapamycin addition together with its corresponding kymographs tracking enrichment of ActA and actin on the membrane in time. t=0 and the dashed black lines on the kymographs represent the rapamycin addition timepoint. B. Tracking the Pearson correlation coefficient between biochemical parameters (ActA and actin) over time highlights no correlation change upon rapamycin addition (top). The Pearson correlation coefficient evolution for ActA and local curvature become further decorrelated upon rapamycin addition (middle). Similarly for actin and local curvature, no correlation is observed (bottom). C. Mean-normalized fluorescence intensity profiles of ActA and actin shown at two frames pre-rapamycin and 10 frames post-rapamycin addition. D. Plots of the entropy of boundary parameters over time, highlighting that ActA entropy remains steady while those of actin and eccentricity both spike after rapamycin addition. Error bars indicate SEM. E. Plots of mean ActA intensity, mean actin intensity, and eccentricity, where the bulk correlation is computed over aggregated data from all GUVs for 18 frames pre-rapamycin and 35 frame post-rapamaycin. For each plot, n= 18.

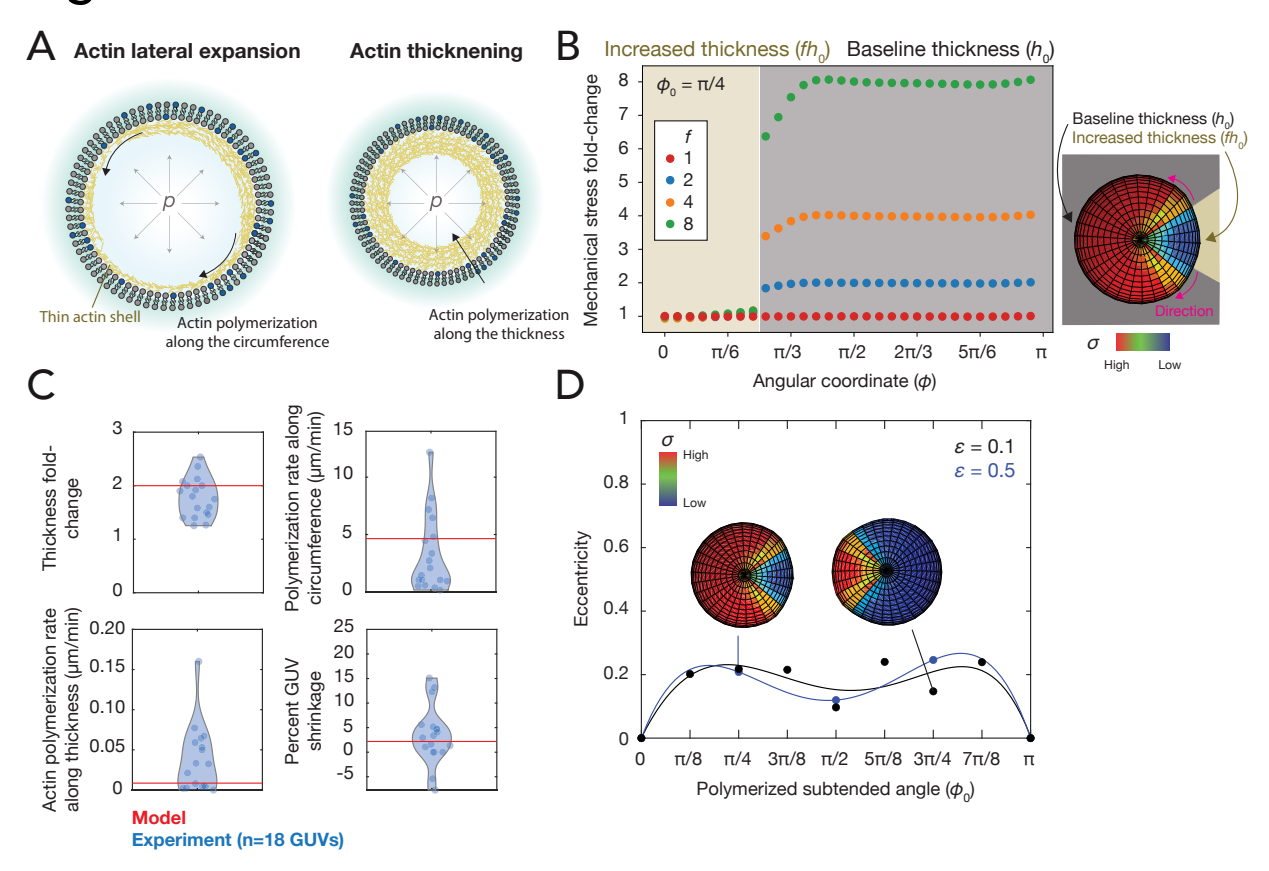


Figure 4. Biophysical modeling of the dynamics and mechanics of actin polymerization. A. Schematic of actin dynamics predicted by the model, in which the volumetric rate of actin polymerization depends on the mechanical stress. Actin polymerization is predicted to predominantly occur along the circumference (lateral expansion), then along the GUV thickness (thickening). The actin is viewed as a thin elastic shell loaded by the internal turgor pressure, p. **B.** Plot of the fold-change in mechanical stress, $\sigma(\varphi)/\sigma_0$, where $\sigma(\varphi)$ is the average maximum principal stress at the angular coordinate φ and $\sigma_0 = pr_0/2h_0$ is the principal stress where the thickness is h_0 . Results are shown for a polymerized subtended angle of $\varphi_0 = \pi/4$ and different thickness factors of f = 1, 2, 4 and 8. (Inset) Representative finite-element simulation results. The maximum principal stress is visualized. **C.** Comparison of model predictions (red lines) with experimental measurements (blue points) for the 18 GUVs analyzed in Fig. 3, for characteristic parameter values of $h_0 = 0.1 \ \mu m$, f = 2, $\ell = 0.1 \ \mu m$, $r_0 = 10 \ \mu m$, $v_0 = 200 \ \text{min}^{-1}$, actin elastic modulus $E = 0.1 \ \text{GPa}$, 66,67 actin Poisson's ratio $\nu = 0$, and turgor pressure $p = 1 \ \text{atm}$. Rates were calculated as linear approximations; see Supplementary Information for details. **D**. Plot of simulated GUV eccentricity values as a function of the polymerized subtended angle, φ_0 , for the same parameter values as in **C**, corresponding to mechanical strains of $pr_0/Eh_0 = 0.1 \ \text{(black)}$. A value of $p = 5 \ \text{atm}$ was also used in the simulations, corresponding to mechanical strains of $0.5 \ \text{(blue)}$.

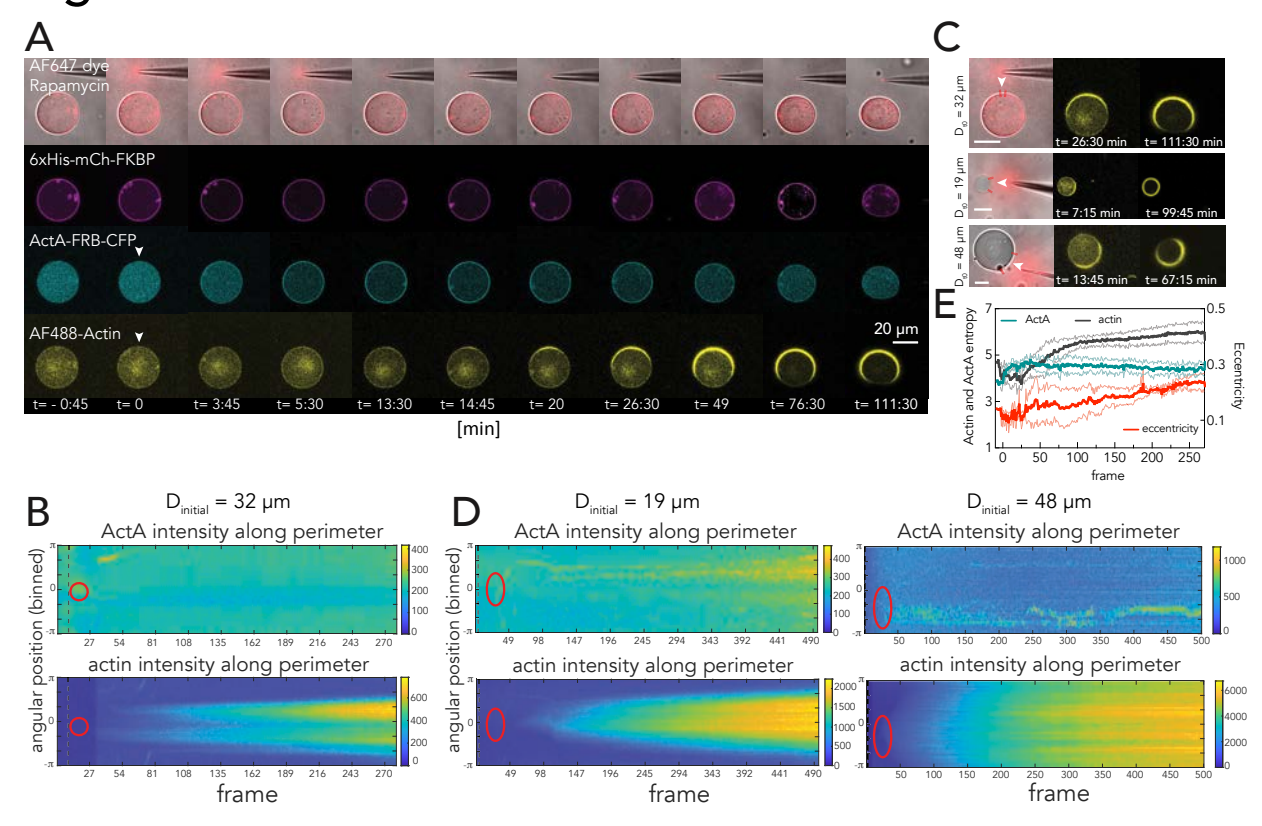


Figure 5. Reconstitution of spatially controlled localized actin deformation. A. Confocal images of GUVs during rapamycin administration. Upon rapamycin release (marked by the pink Alexa fluor 647 dye signal), ActA first translocates to the location marked by the white arrow. Local F-actin appears at the same site within \sim 15 min. B. Kymographs showing the evolution of the ActA and actin signal intensity on the membrane for the GUV presented in (A). The red oval marks the effective high rapamycin concentration area. C. Comparison of the actin thickening versus spreading, for GUVs of different radii. The area between the two lines highlights the effective rapamycin area. Scale bar is 20 μm . D. Similar to (B), but showing a kymograph of the signal accumulation for the 48 μm and 19 μm GUVs depicted in (C). Time 0 corresponds to the rapamycin input addition. E. Plots of the entropy of boundary parameters over time, highlighting that ActA entropy remains steady while that of actin and eccentricity both spike after rapamycin addition. Error bars indicate SEM.

Table 1

Table 1 | Biomolecular modules used in the active protocells

	Part	Function	Concentration
Protein Network	6xHis-mCherry-FKBP	chemical sensing - membrane anchorin	g 9.5 μM
	ActA-FRB-CFP	chemical sensing - Arp2/3 activation	2-8.5 μM
	Arp2/3 complex	actin nucleation	0.15 - 0.5 μM
	G-actin	force generation	1.5-3 μM
Lipids	POPC	biological membrane mimic	94 mol%
	DGS-NTA(Ni)	anchoring sensory modules	5 mol%
	PEG	reducing unspecific lipid-protein interac	tion 1 mol%
Inner Buffer	ATP MgCl ₂ KCl Tris-HCl (pH 7.5) sucrose	energy source actin stability and polymerization physiological salt pH stability osmotic pressure balance	1 mM <1 mM <50 mM >10 mM 850 mM

Table 1. Molecular constituents of protocells.

Supplementary Materials

Synthetic control of actin polymerization and symmetry breaking in active protocells

This PDF file includes:

- Supplementary Text
- Supplementary Figures 1 to 12
- Supplementary Tables 1 to 2
- Supplementary Movies 1 to 3 Captions

Other Supplementary Materials for this manuscript include the following:

• Supplementary Movies 1 to 3

Supplementary Text

Plasmid construction

Twin-Strep-tag®-pET28 was a kind gift from Dr. Kanemaki. pQE-80L-based plasmids and SspB sequences were obtained from pQE-80L MBP-SspB Nano (Addgene #60409). Mammalian expression plasmids and ECFP, EYFP, and mCherry sequences were constructed and obtained from pECFP-C1, pEYFP-C1, and pmCherry-C1 (Clontech). The mActA(1-183) sequence was PCR- amplified from the plasmid reported previously. The beta-actin sequence was obtained from paGFP-actin plasmid, as previously reported (80). MARCKS and Fyn sequences were synthesized by oligo DNA annealing.

Protein expression and purification

6xHis-YFP-FKBP (pET28a) We transformed YFP-FKBP in BL21 (RIL) cells and set up an overnight, 37 °C, 220 rpm culture of one colony in 5 mL of LB media supplemented with kanamycin and chloramphenicol. The next day, we transferred the 5 mL culture to 1 L of LB media supplemented with kanamycin and chloramphenicol at the same growth condition. Cells were induced at OD_{600} of 0.5 with 400 μM IPTG, and the temperature was reduced to 19 °C for overnight growth. Cells were harvested the next day, resolubilized in lysis buffer (10 mM Tris-HCl pH 7.4, 50 mM NaCl, 10 mM imidazole, 10 mM β-mercaptoethanol, 10% V/V glycerol), and lysed with the microfluidizer. Lysate was spun at 20,000x g for 40 min to isolate the soluble fraction, and cleared with 0.2 μm filter. The soluble fraction was loaded on Ni-NTA beads (GE Healthcare) and washed with 15 column volumes wash buffer (10 mM Tris-HCl pH 7.4, 500 mM NaCl, 10 mM imidazole, 10 mM β-mercaptoethanol, 10% V/V glycerol). An FPLC was used to administer an imidazole linear gradient at 200 mM imidazole peak (10 mM Tris-HCl, 100 mM NaCl, 200 mM imidazole, 10 mM β-mercaptoethanol, 10% V/V glycerol). The purest fractions (assessed by SDS-PAGE gel) were harvested and dialyzed overnight in storage buffer (10 mM Tris-HCl pH 7.6, 50 mM NaCl, 10% V/V glycerol, 1 mM DTT). Protein was concentrated (Amicon Ultracentrifugation), snap frozen, and stored at -80 °C.

6xHis-CFP-FRB (pET28a) We transformed CFP-FRB in BL21 (RIL) cells and inoculated one colony in 5 mL of LB supplemented with kanamycin media and grew at 37 °C, 220 rpm, overnight. 5 ml of the overnight culture was added to 1L of LB/kanamycin media and induced with 400 μM IPTG when OD_{600} reached 0.5. Growth was continued at 19 °C overnight and cells harvested the next day, resolubilized in lysis buffer, and lysed with a microfluidizer. Lysate was spun at 20,000g for 40 min and the soluble fraction collected. To pellet down DNA, 5% W/V polyethyleneimine was gradually added and spun at 15,000g for 5 minutes. The supernatant was collected and saturated ammonium sulfate added for a final concentration of 40%, spun at 10,000g for 10 minutes. Pellet was resuspended in storage buffer. We then dialyzed the protein overnight to remove excess ammonium sulfate and used Ni-NTA column for the remaining purification steps similar to what is detailed for YFP-FKBP construct.

6xHis-mCherry-FKBP (pBiEx) and 6xHis-mCherry-FKBP-MARCKS (pBiEx) BL21-RIL cells were transformed. 10 ml of overnight LB/ampicillin culture was grown at 37 °C and 220 rpm was transferred to 1L of the same media for next day expression at 37 °C. Due to high level of leaky expression, no further IPTG induction was implemented. The culture was harvested after 15-20 hours of growth when the media color looked brightly pink. Cells were resolubilized in the lysis buffer (50 mM Tris-HCl pH 7.9, 100 mM NaCl, 1 mM EDTA, 10% glycerol, 10 mM β-Mercaptoethanol, Roche EDTA-free protease inhibitor), lysed with the microfluidizer, spun at 20,000g for 40 min and the soluble fractions were harvested. Ni-NTA purification proceeded similar to what is detailed for YFP-FKBP.

6xHis-mActA (1-584)-FRB-CFP (pET28a) We inoculated a colony of BL21-CodonPlus(DE3)-RIL competent cells (Agilent Technologies 230245) transformed with the plasmid DNA in 10 ml of LB media supplemented with kanamycin and grew overnight at 37 °C, 220 rpm. Culture was transferred to 1L of LB/kanamycin and expanded at 37 °C, 220 rpm till OD_{600} reached 0.5. Cells were induced with IPTG at a final concentration of 0.4 mM and culture continued at 19 °C, 220 rpm, overnight. The cells were pelleted at 4500g, 4 °C for 15 min and the pellet resolubilized in 20 ml of lysis buffer (10 mM Tris pH 7.6, 100 mM NaCl, 10 mM imidazole, 10% glycerol, 1 mM β-mercaptoethanol and cOmplete EDTA-free protease inhibitor tablet (Sigma-Aldrich 11836170001). Cells were lysed with a microfluidizer and the soluble fraction harvested by centrifugation at 16,000g, 4 °C for 40 min. The supernatant was filtered with 0.2 μm syringe filters (Thermo Scientific F25006). We equilibrated a 5 ml His-Trap HP column (GE Life Sciences) with the lysis buffer lacking protease inhibitors and eluted the protein using a linear imidazole gradient from 50-500 mM over 20 column volumes. The eluted fractions were analyzed on a SDS-PAGE gel and subsequently the peak fractions detected on the Coomassie blue (Biorad 1610400) stained gel were pooled and dialyzed in a 10 kDa SnakeSkin dialysis tubing (Thermo Fisher Scientific 68100) in 2L of storage buffer (10 mM Tris-HCl pH 7.6, and 50 mM NaCl, 10% glycerol,

and 1 mM β -mercaptoethanol) at 4 $^{\circ}$ C, overnight. The next day the protein was dialyzed for an additional 3 hours in fresh storage buffer and subsequently applied to a Superdex 200 10/300 GL (GE Life Sciences) equilibrated in the same buffer. The peak fractions were combined, and concentrated with an Amicon® Ultra 10 kDa centrifugal filter unit (Millipore UFC801024). Aliquoted protein vials were flash-frozen and stored at -80 $^{\circ}$ C.

2xstrep-ActA(1-183)-FRB-CFP (Twin-Strep-tag®-pET28) Inoculation and growth was similar to the ActA(1-584)-CFP-FRB construct. For lysis we used 100~mM Tris-HCl pH7.4, 150~mM NaCl, and cOmplete™ EDTA-free protease inhibitor. The cells were lysed with a microfluidizer, and the supernatant clarified as previously detailed. Strep-tactin XT (GE Healthcare) beads were equilibrated with 100~mM Tris-HCl, 150~mM NaCl, 1~mM EDTA, pH 8.0 and the cleared lysate was passed through the column and washed with 10~c0 column volumes of the same buffer. Protein was eluted with 100~mM Tris-HCl, 150~mM NaCl, 1~mM EDTA, and 50~mM biotin at differential elution volumes recommended by the manufacturer, dialyzed against storage buffer (10~mM Tris-HCl, 50~mM NaCl, 10% glycerol, 1~mM DTT) overnight, concentrated, and froze down in individual vials the next day.

Actin One milligram of actin (Cytoskeleton Inc. AKL99-B) was dissolved in 400 μ L G-buffer (2 mM Tris-HCl (pH 7.5 at RT), 0.1 mM CaCl2, 0.2 mM ATP, 0.5 mM DTT, 1 mM NaN₃) and dialyzed against the same buffer. After 3 days dialysis with daily buffer exchange, the actin was purified by Superdex 200 Increase 10/300 GL column (GE Healthcare) to separate monomer fraction from occasional larger size (smaller elution volume) fraction. The purified actin was stored at 4 $^{\circ}$ C and dialyzed against the G-buffer that was refreshed twice a week.

Cap32/34 (pET14b) Cap32 and Cap34 proteins were individually expressed in LB/Amp culture (conditions similar to CFP-FRB). The pellets were pulled together after resolubilization in the lysis buffer (used for CFP-FRB) to form the Cap32/34 complex. Ni-NTA column was used for purification followed by size exclusion column to isolate the protein complex fractions.

FRET assay in the GUVs

 $3~\mu M$ CFP-FRB and $3.4~\mu M$ YFP-FKBP were reconstituted in PBS buffer inside symmetric GUVs with POPC membrane. For osmotic pressure balance fsupp 750~mM sucrose was present in the GUVs while outside buffer was PBS buffer with 750~mM glucose. An inverted epi-fluorescence microscope (Axiovert135TV, ZEISS) with $40\times$ oil objective was used to take images at one frame per 30 seconds prior to and post-rapamycin and DMSO (control) administration. CFP, YFP, and FRET intensities were measured. The FRET signal was reported after normalizing against the CFP donor signal. Image processing was performed using the MetaMorph® software (Molecular Devices). To account for photobleaching, the decay in fluorescence signal 10 min prior to input addition was measured and the data were corrected approximating photo bleaching as a linear trend.

Pyrene assay

Pyrene-actin polymerization assay was performed with FluoroMax 3 and Datamax software. Pyrene fluorescence and its kinetics were measured by 365~nm emission (1 nm bandwidth) and 497~nm excitation (5 nm bandwidth). Actin and pyrene-labeled actin were mixed in G-buffer to make 5% pyrene actin. Arp2/3 and GST-WASP-VCA were reconstituted as described in the manufacturer's protocols and diluted to desired concentration with F-buffer (10 mM Tris-HCl (pH 7.5 rt), 50~mM KCl, 2~mM MgCl2, 1~mM ATP). Reaction mixture was prepared as indicated in figure legends and the reaction was performed at room temperature. Reaction was started with 1 μ M actin and 10 nM Arp2/3 solution in F-buffer. GST-WASP-VCA or ActA variants (final 100~nM) were added at time = 0. Reaction was started with 1 μ M actin in F-buffer. Arp2/3 (final 10~nM) and GST-WASP-VCA or ActA variants (final 800~nM) were added at time = 0.

Image processing and analysis

Kymograph generation To generate the kymographs, an initial list of finely and equally spaced boundary points were computed using a snake algorithm for each frame based on the segmentation mask. A 2-D Savitzky-Golay filter was applied to generate a smooth boundary for estimating biophysical boundary quantities. Biochemical quantities (membrane marker, ActA, actin) were estimated at each boundary point as the mean of the background-subtracted fluorescence intensity along a short line segment perpendicular to the boundary. For the kymographs used in PCA analysis, biochemical quantities were quantified as boundary:lumen ratios by normalizing the fluorescent signal at a given boundary point (computed as before) to the background-subtracted fluorescent signal in the lumen (computed as background-subtracted mean of the bottom 20% of signal values in a mask defining the GUV lumen). Local curvature was approximated as 1/radius of the circle with best geometric fit for a local set of boundary points (code from MATLAB

file exchange). To generate final kymographs with a fixed number of points for all subsequent analysis, the list of biophysical quantities initially estimated over the smooth, dense boundary points was sub-sampled at 360 equally spaced angular bins from $-\pi$ to π .

Measurement of actin spreading rate To estimate radial actin polymerization rate standard kymographs of actin fluorescent signal from 360 angular bins were analyzed. To obtain a smooth actin patch for analysis, a variety of standard smoothing steps were performed. A 21-point moving average window in space was applied, followed by 2D Gaussian and median filtering. The actin patch was then segmented using intensity thresholding, morphological operations, and active contours technique. The boundary of the segmented actin patch was finally smoothed using a 2D Savitzky-Golay filter. A portion of the boundary points were then fit to a line using least squares regression. The slope provides an estimate of the average rate of actin polymerization. Linearized rates of actin thickness increase were estimated by measuring the number of pixels with high fluorescent YFP intensity in a randomly selected actin cross section at time t', subtracting the corresponding initial value, and dividing by t'.

Correlation analysis For tracking correlations between local biophysical quantities in individual GUVs over time, the Pearson correlation coefficient was computed for pairs of biophysical quantities (ActA-actin; ActA-curvature; actin-curvature) over 360 boundary points at each frame (a single column in a kymograph). To minimize the effect of artificial correlations due to membrane artifacts, an inclusion criteria for both spatial points and frames was used: 1) only include spatial points with membrane marker signal in bottom 75th percentile for a given GUV, and 2) only include frames with at least 180 points. All available GUVs (n=18) were utilized in this analysis.

The evolution of asymmetry in biochemical parameters and global shape changes in individual GUVs over time were assessed using two quantities: the entropy of biochemical signal values, and the eccentricity of the GUV. Changes in entropy, computed in the information theory sense, as a measure of signal randomness, provided an indirect measure of changes in symmetry. The input space of biochemical signals from all frames of an individual GUVs kymograph was first discretized into 256 bins for consistent 8-bit representation. For each GUV, the entropy for a given biochemical quantity at the jth frame, $X^{(j)}$, was then computed in the information theory sense as $H(X^{(j)}) = \sum_i p_i log_2(p_i)$, for all $p_i > 0$, where $p_i = P(X^{(j)} = x_i)$ is the probability of the ith bin of signal values. The probability distribution for $X^{(j)}$ was computed from the histogram of discretized signal values at frame j. Fixed spatial discretization at each frame (360 spatial points) and fixed signal discretization (8-bit) ensured consistency with entropies remaining between 0 and 8 over all frames and all GUVs. For tracking global shape at each frame, MATLAB's built-in function was used to compute eccentricity, defined as the ratio of the focal length to the major axis length of the ellipse that best fits the GUV mask. Note that eccentricity values range from 0 (perfect circle) to 1 (line segment). All available GUVs (n=18) were utilized in this analysis.

To compare fluorescent intensity profiles of ActA and actin from different GUVs before and after rapamycin, two time points were selected: two frames before rapamycin addition, and 10 frames after rapamycin addition. At each frame, the mean-normalized fluorescent intensity profiles of ActA and actin across 360 spatial points were plotted. All available GUVs (n=18) were utilized in this analysis.

Bulk correlation analysis was used to assess biophysical trends in data from multiple GUVs (n=17) and multiple frames. Initially, biochemical kymographs were max-normalized for proper comparisons across GUVs. For ActA-actin bulk correlation analysis, the kymographs were split into a pre-rapamycin section (frame 1 to last frame before rapamycin; length varies by GUV but ranges from 6-18 frames) and a 35-frame post-rapamycin section (10 frames after rapamycin to 44 frames after rapamycin). Pearson correlation coefficients were computed for pairs of ActA and actin values in these sections from multiple GUVs. To minimize the effect of artificial correlations due to membrane artifacts, an inclusion criteria for spatial points was used: only include points with membrane marker signal in bottom 75th percentile for a given GUV.

For ActA-eccentricity and actin-eccentricity bulk correlation analyses, the mean of the biochemical signals from 360 spatial points was first computed at each frame. This scalar conversion of biochemical signals was necessary for comparison with the eccentricity, a scalar shape parameter. Additionally, all 360 points were included for scalar conversion; no inclusion criteria based on membrane marker was employed. Pre-rapamycin sections for each GUV were defined as before; however, post-rapamycin section was defined as a 35-frame window from 20 frames after rapamycin to 54 frames after rapamycin. Pearson correlation coefficients were then computed for pairs of biophysical quantities (mean ActA-eccentricity; mean actin-eccentricity) in these sections and multiple GUVs.

Principal component analysis Prior to applying principal component analysis (PCA) analysis on kymographs from multiple GUVs, steps were taken for signal normalization and spatiotemporal alignment. For ActA and actin, boundary:lumen ratio based kymographs were used, with max-normalization for each GUV. For curvature kymographs, the local curvature was normalized to an approximate bulk initial curvature for each GUV. This bulk initial curvature was approximated as $\frac{1}{0.5L}$ where L is the major axis length of the best-fit ellipse for the GUV shape at the first frame after rapamycin. Spatial points from all kymographs were binned from 360 points to 180 points using averaging. Smoothing was performed using a 21-point moving average window in space. Spatial alignment of kymograph data from globally stimulated GUVs (n=17) was approached by first centering each GUV's actin kymograph to the spatial point (corresponding to an angular direction) with maximum value at 35 frames post-rapamycin. This centering direction was then applied to the ActA and curvature kymographs for comparison of patterns across biophysical parameters. Temporal alignment was performed by simply selecting a 50-frame window from frame 1 post-rapamycin to frame 50 post-rapamycin. For locally stimulated GUVs (n=3), all kymographs were spatially aligned and centered to the direction of the external micropipette; and temporal alignment was performed by selecting a 250-frame window, from frame 1 post-rapamycin to frame 250 post-rapamycin.

PCA was then performed using singular value decomposition of the matrix of mean-subtracted, aligned, vectorized 2-D kymographs. This matrix has 17 columns for the global rapamycin data and 3 columns for local rapamycin data, from the 17 GUVs and 3 GUVs analyzed respectively for each dataset. Principal components (PCs) were re-shaped into the dimensions of the 2-D kymographs for visualization of dominant spatiotemporal trends in kymographs. Cumulative sums of the square of the singular values were used to compute percent variance captured by the corresponding top PCs.

Model of actin polymerization dynamics

As discussed in the main text, we assume that, due to baseline levels of spontaneous (rapamycin-independent) actin polymerization, there already exists a spherical shell layer of actin anchored to the inner leaflet of the vesicle. ⁶⁹ This actin shell will be the main load-bearing element, and will be remodeled by additional (rapamycin-dependent) polymerization (Fig. 4a of the main text). While characteristics including actin flow ²⁵ may also be important, here we focus on the elastic stretching stresses in the actin shell that are generated by the outward turgor pressure.

Suppose there is a nucleation site (a subsurface of the sphere) at which increased actin polymerization occurs. Any point on this site is given by surface coordinates, (θ,φ) , where $\theta\in[0,2\pi]$ and $\varphi\in[0,\pi]$ span the sphere. We assume that the volume, V, of polymerized actin is increased locally at this nucleation site. As described in the main text, we may consider a model in which the local, volumetric rate of actin polymerization at any coordinate (θ,φ) contained within the nucleation site quantitatively depends on the mechanical stress:

$$\frac{dV(\theta,\varphi,t)}{dt} = \ell^3 v_0 e^{\sigma(\theta,\varphi,t)/\sigma_0}.$$
 (2)

Here, ℓ^3 is the volume of an effective unit actin insertion with edge length ℓ , v_0 is a baseline actin polymerization rate with units of 1/min (which may depend on upstream nucleation factors such as Arp2/3 and Barb), and σ_0 is a baseline value of mechanical stress at the nucleation site. Eq. (2) is the basic assumption of our model; namely, that actin polymerization at the nucleation site is spatially coupled to mechanical stress, and more actin polymerization occurs at regions of larger tensile stress. We note, in turn, that mechanical stress is trivially coupled to actin polymerization because the shell thickness changes as $dh(\theta,\varphi,t)/dt=\ell^{-2}dV(\theta,\varphi,t)/dt$: since we expect the mechanical stress to scale as pr/h, where r is the radius and h is the thickness, there is less mechanical stress at regions of larger thickness. We note that Eq. (2) makes an assumption similar to Eq. (3) in ref., 52 in which the authors assumed that the actin polymerization rate outside a droplet, with actin polymerizing in only one direction, depends on the normal stress in the droplet: the functional form of the stress-dependence is a Kramer's rate. The main difference with respect to our Eq. (2) is that Eq. (2) considers the in-plane, not normal, stresses, and that actin polymerization will occur in three dimensions.

In Fig. 4 of the main text, we have plotted σ as the maximal principal stress of the actin shell as a simple scalar measure of tension:

$$\sigma_{\mathsf{M}} = \mathsf{max}(\sigma_{xx}, \sigma_{yy}). \tag{3}$$

where σ_{xx} and σ_{yy} are the nonvanishing components of the stress tensor in the orthogonal coordinate system (x,y). Nevertheless, it is straightforward to see that our results hold for other stress measures.

We will show that, with the assumption of Eq. (2), the model predicts the lateral and normal modes of actin polymerization, and also the observed vesicle shrinkage. We first estimate the mechanical stress, $\sigma(\theta, \varphi, t)/\sigma_0$.

Determination of the mechanical stresses in an axisymmetric polymerizing actin shell

We first determine the mechanical stress in the polymerizing actin shell. This analysis will reveal that, when actin polymerizes locally at a nucleation site, the mechanical stresses at the nucleation site are largest at the edges. Accordingly, from Eq. (2), the direction of fastest polymerization will be lateral on the surface of the vesicle. Furthermore, we will quantitatively determine the magnitude of stress increase, which will dictate the value of the $e^{\sigma(\theta,\varphi,t)/\sigma_0}$ term in Eq. (2) and allow for the estimation of v_0 from experimental data.

We assume that polymerized actin forms a linear-elastic, isotropic, spherical shell anchored to the inner leaflet of the vesicle. Denote the radius, thickness, three-dimensional Young's modulus, and Poisson's ratio of this shell as r, h, E, and ν , respectively. This shell resists an internal (osmotic) pressure of p. If the shell thickness, h, is constant, then we know from thin shell theory that the stresses, σ , and strains, ε , in an orthogonal coordinate system, (x, y), are

$$\sigma_{xx} = \sigma_{yy} = \frac{pr}{2h}, \quad \sigma_{xy} = 0, \quad \varepsilon_{xx} = \varepsilon_{yy} = \frac{\sigma}{E}(1 - \nu) = \frac{pr(1 - \nu)}{2Eh}, \quad \varepsilon_{xy} = 0.$$
 (4)

The introduction of a nucleation site results in actin polymerization on a patch of this shell. This increases the actin thickness, h, locally, so that h is no longer a constant but varies in space and time. Let us assume, for simplicity, that actin polymerization increases h axisymmetrically (independent of θ) beyond a baseline value, h_0 , by a constant fold amount, f. Under the assumption of constant f, $h(\theta, \varphi, t) = h(\varphi, t)$ depends only on the subtended angle φ as follows:

$$h(\varphi,t) = \begin{cases} fh_0 & \varphi < \varphi_0(t) \\ h_0 & \varphi \ge \varphi_0(t). \end{cases}$$
 (5)

In particular, the spherical shell transitions from a thickness of h_0 to a thickness of h_0 at the angle $\varphi_0(t)$, and this angle increases in time; ultimately, if actin polymerizes faster laterally than in the thickness direction, the entire shell will have thickness $\approx fh_0$ due to the lateral actin polymerization.

In the bulk of the two caps $(\varphi \ll \varphi_0(t), \varphi \gg \varphi_0(t))$, we expect analogous equations to Eq. (4) to hold because the thickness change is only at the interface. The mechanical stress at the interface may be more subtle because of this thickness change. We anticipate that the stresses will increase from $\sigma_{xx} = \sigma_{yy} = pr/2fh_0$ to $\sigma_{xx} = \sigma_{yy} = pr/2h$ at the interface. In confirmation of this, we used finite-element simulations (Abaqus FEA) to model the stresses at the interface. Simulating the mechanical stresses across different values of f and φ_0 , the results consistently revealed that the stresses at $\varphi = \varphi_0$ increases from the stresses in the thicker region to the stresses in the thinner region (Fig. 4b of the main text). Based on these results, and normalizing with respect to the baseline stress $\sigma_0 = pR/(2fh_0)$ at the nucleation site, we find that for $\varphi \leq \varphi_0$,

$$\frac{\sigma(\theta, \varphi, t)}{\sigma_0} \approx \begin{cases} 1 & \varphi < \varphi_0(t) \\ f & \varphi = \varphi_0(t). \end{cases}$$
 (6)

In other words, the fold-change in stress is maximal at the edge of the nucleation site and is approximated by the fold-change, f, in actin thickness. f can be measured from the experiments by comparing the thickness from the actin fluorescence before and after lateral actin polymerization.

Determination of the lateral and normal actin polymerization rates

Based on the considerations above, the exponential term in Eq. (2) will be constant in time at the expanding front ($\varphi = \varphi_0$), and the term will be approximately e^f . Thus, for $f \gg 1$, the model predicts that actin polymerization will occur mostly laterally whenever there is differential stress in the actin shell. When the actin shell becomes uniform in thickness (under our simplifying assumptions, with a thickness of fh_0), there is no differential stress and $\sigma(\theta,\varphi,t)/\sigma_0=1$; accordingly, the polymerization is expected to occur in the normal, out-of-plane direction, and its rate decreases by a factor of e^{f-1} . This can be summarized as follows:

$$\frac{dV(\theta, \varphi, t)}{dt} \approx \begin{cases} \ell^3 v_0 e^f & \varphi = \varphi_0(t) \\ \ell^3 v_0 e & \varphi < \varphi_0(t). \end{cases}$$
 (7)

Using this equation, we can determine how the actin circumference and thickness should increase in time.

During lateral actin polymerization, the area that is added laterally (at $\varphi = \varphi_0$) to the actin shell is added at any angle θ with rate

$$\frac{dA(\theta,t)}{dt} = \frac{1}{\ell} \left. \frac{dV(\theta,\varphi,t)}{dt} \right|_{\varphi=\varphi_0} \approx \ell^2 v_0 e^f, \tag{8}$$

so the total lateral polymerized area at θ after time t is

$$A(\theta, t) = \ell^2 v_0 e^f t. \tag{9}$$

The total area of an axisymmetric spherical cap of depth d is $2\pi rd$. Integrating $A(\theta,t)$ over $\theta\in[0,2\pi]$ and setting the two areas equal, the total polymerized depth after time t is $d(t)=\ell^2v_0e^ft/r$. The angle subtended by the axisymmetric spherical cap is $\varphi_0(t)=\cos^{-1}[(r-d)/r]$. Taking r to be constant and approximated by r_0 (which is valid for small deformations and for the short timescale of lateral actin polymerization), the total polymerized circumference at time $t\leq \varphi_0^{-1}(\pi)$ is then

$$C(t) = C_i + 2\pi r \times \frac{\varphi_0(t)}{\pi} = C_i + 2r\cos^{-1}\left(1 - \frac{d(t)}{r}\right) = C_i + 2r\cos^{-1}\left(1 - \frac{\ell^2 v_0 e^f t}{r^2}\right),\tag{10}$$

where C_i is a constant initial value (and will hereafter be taken as 0). Note that $\varphi_0^{-1}(\pi)$ is the time at which lateral polymerization completes, and the entire circumference is covered with the laterally polymerized actin.

Although most of the actin will polymerize laterally (under the assumption that $f \gg 1$), there is also normal, out-of-plane polymerization in the bulk of the nucleation site ($\varphi < \varphi_0$). The volume that gets added to the actin shell at any coordinate $(\theta, \varphi), \varphi < \varphi_0(t)$, is added with rate

$$\frac{dV(\theta,\varphi,t)}{dt} \approx \ell^3 v_0 e. \tag{11}$$

Integrating over $\theta \in [0, 2\pi]$, $\varphi \in [0, \varphi_0(t)]$, and t, the volume added by this mode of polymerization after time t is

$$2\pi\ell^3 v_0 e \int_{t'=0}^t \cos^{-1}\left(1 - \frac{\ell^2 v_0 e^f t'}{r^2}\right) dt',$$

which can be calculated numerically. Distributing this volume over the subtended surface area of $2\pi rd$, the average thickness of the laterally polymerized actin increases as

$$h(t) = h_i + \frac{\ell}{e^{f-1}t} \int_{t'=0}^t \cos^{-1}\left(1 - \frac{\ell^2 v_0 e^f t'}{r^2}\right) dt', \quad t \le \varphi_0^{-1}(\pi), \tag{12}$$

where $h_i = fh_0$ is a constant initial value. For $f \gg 1$, the second term becomes vanishingly small and is dominated by the first term. Thus, the thickness increase does not significantly increase the ratio $h(t)/h_0$ beyond f during lateral polymerization, indicating the self-consistency with assuming f to be constant in the limit of large f.

Similarly, during the normal, out-of-plane polymerization which occurs after the actin shell has uniform thickness, $\varphi_0 = \pi$, d = 2r, and the average thickness of the polymerized actin increases as

$$h(t) = h'_i + \frac{\pi \ell^3 v_0 e t}{2r^2}, \quad t > \varphi_0^{-1}(\pi),$$
 (13)

where $h'_i = h(\varphi_0^{-1}(\pi))$ is a constant initial value.

Determination of the radial shrinkage rate during actin thickening

As actin polymerizes uniformly, the thickness of the actin shell increases as given by Eq. (13). The strain is given by Eq. (4) and decreases in time:

$$\varepsilon(t) = \frac{pr(1-\nu)}{2Eh(t)} = \frac{pr(1-\nu)}{2E(h'_i + \pi \ell^3 v_0 et/(2r^2))} \approx \frac{pr_0(1-\nu)}{2E(h'_i + \pi \ell^3 v_0 et/(2r_0^2))}.$$
 (14)

In the above, we have assumed that r is constant and approximately r_0 , which is valid for small deformations and on the short timescale of lateral polymerization; deviations from this assumption will lead to minor corrections in the strain, which can be discarded for our parameter values of interest. Accordingly, with the typical linear strain-displacement relation, the model predicts the rate of shrinkage as:

$$\frac{r(t)}{r_0} = 1 + \varepsilon(t). \tag{15}$$

Comparison to experimental data

The main predictions of our model are the following:

$$\frac{C(t)}{2\pi r} = \frac{1}{\pi} \cos^{-1} \left(1 - \frac{\ell^2 v_0 e^f t}{r_0^2} \right), \quad h(t) = h_i' + \frac{\pi \ell^3 v_0 e t}{2r_0^2} \ (t > \varphi_0^{-1}(\pi)), \quad \frac{r(t)}{r_0} = \frac{p r_0 (1 - \nu)}{2Eh(t)}. \tag{16}$$

- The first equation describes the time-evolution of the fraction of the vesicle contour that is covered by actin polymerizing on a nucleation site.
- The second equation describes the time-evolution of the average actin thickness. At times longer than the time it takes for the actin to extend around the circumference $(t>\varphi_0^{-1}(\pi))$, the thickness growth is linear in time, and actin polymerizes in the normal direction, uniformly over the entire surface.
- The third equation describes the radial shrinkage associated with the increase in thickness.

We anticipate that all parameters can be measured from the experiments, and that the only fitting parameter is v_0 , the baseline rate of actin polymerization (with units of min⁻¹).

To compare with the experiments:

- We measured the thickness (in μ m) across which actin fluoresces at the vesicle contour, and found that the fold-change in actin thickness during lateral polymerization was $f\gtrsim 2$. After a point on the vesicle circumference is covered by the laterally polymerizing actin, the thickness further increases slightly (order of \sim 0.1-1 \times) during this first phase of polymerization.
- We measured the vesicle radius, r, from either the phase-contrast or fluorescence (when phase-contrast not available) timelapse. We then used a linear approximation for the lateral polymerization rate as $2\pi rs/t_{\rm cir}$, where $s\in[0,1]$ is the fraction of the circumference polymerized and $t_{\rm cir}$ is the time (min) needed to finish lateral polymerization (estimated in our model by $\varphi_0^{-1}(\pi)$).
- We measured actin thickness, h, across time in the fluorescence timelapses. We then used a linear approximation for the rate of thickness increase as $\Delta h/\Delta t$, where Δh is the difference in actin thickness between the end of the timelapse ($t_{\rm final}$) and the end of lateral polymerization ($t_{\rm cir}$).
- Finally, we measured the radial shrinkage to be the fractional decrease in radius between the initial and final times.

For comparison, the model predictions for characteristic parameter values are shown in Fig. 4c of the main text. In particular, based on our empirical observations we assume that f=2, $h_i=\ell=0.1~\mu\text{m}$, $r_0=20~\mu\text{m}$.

- We estimate v_0 by approximating the lateral expansion velocity shown in the empirical data in Fig. 4c of the main text, which suggests $v_0 \approx 200 \, \mathrm{min}^{-1}$: this value predicts that actin polymerization would cover the vesicle contour after $\varphi_0^{-1}(\pi) \sim 15 \, \mathrm{min}$, a timescale consistent with experiments.
- Over a longer timescale of \sim 100 min, h(t) is predicted to increase \sim 10-fold to a value of \sim 1 μ m, consistent with the lower end of the rates of thickness increase observed in experiments. It is possible that increases in thickness increase could occur if the rate of actin polymerization was not constant but accelerated in time—for instance, by depending on the amount of polymerized actin.
- Finally, assuming a typical actin Young's modulus of E=0.1 GPa, actin Poisson's ratio of $\nu=0$, and an osmotic pressure of p=1 atm (corresponding to an osmolyte concentration gradient of \sim 50 mM), at long times for which the mechanical strains approximately vanish, the radial shrinkage is predicted to be \sim 5%.

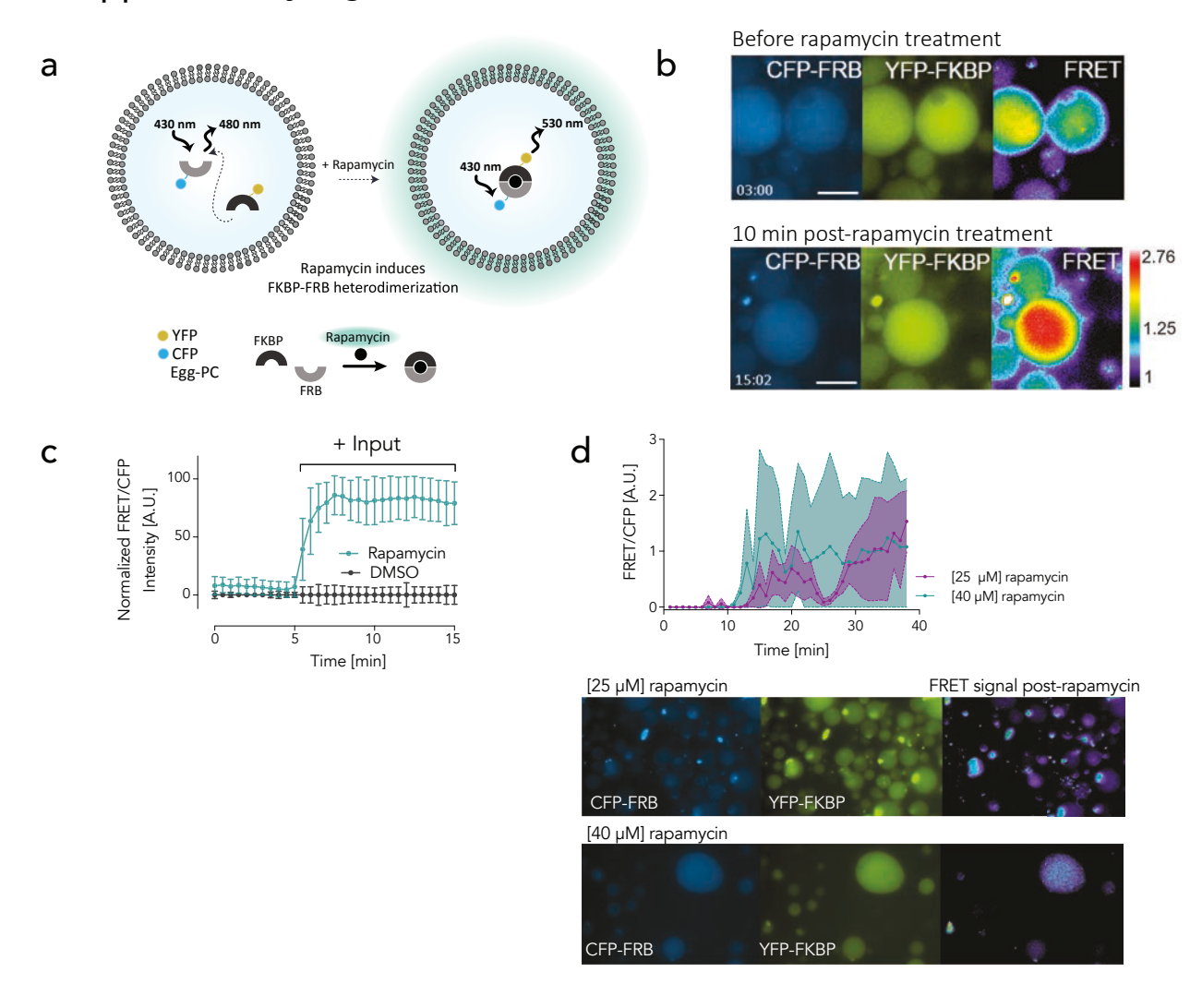
While the model is quantitatively consistent with the different dynamics observed in the experiments, we note here that it is also possible that differences can arise from the limitations of using a linear theory of elasticity, which assumes small deformations.

Predicting eccentricity through mechanical deformations

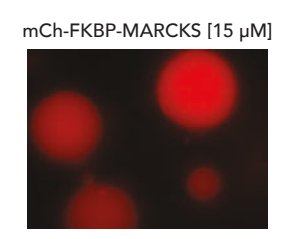
The above analysis assumed that the vesicle was spherical in order to model actin polymerization dynamics. Our empirical analyses further suggest that there is substantive eccentricity in vesicles (Fig. 3d of the main text). In order to determine whether this eccentricity might arise as a result of asymmetric actin polymerization, we modeled the presence of different actin cap shapes. Fig. 4d of the main text shows the result of Abaqus FEA simulations for strains of the order of \sim 0.1 and actin caps with different polymerized subtended angles, φ_0 . For these characteristic values, we found considerable eccentricity, on the order of \sim 0.2 in the deformed shapes.

For all Abaqus FEA analyses performed in this work (as shown in Fig. 4 of the main text), spherical shells of radius 1, each containing 900 finite elements (a 30×30 discretization of $\theta, \varphi \in [0, 2\pi] \times [0, \pi]$) were generated and modeled with an elastic material with dimensionless elastic modulus 1. The baseline thickness of the shell was set to 0.02, and dimensionless pressure loads of 0.002 or 0.01 were applied.

Supplementary Figure 1



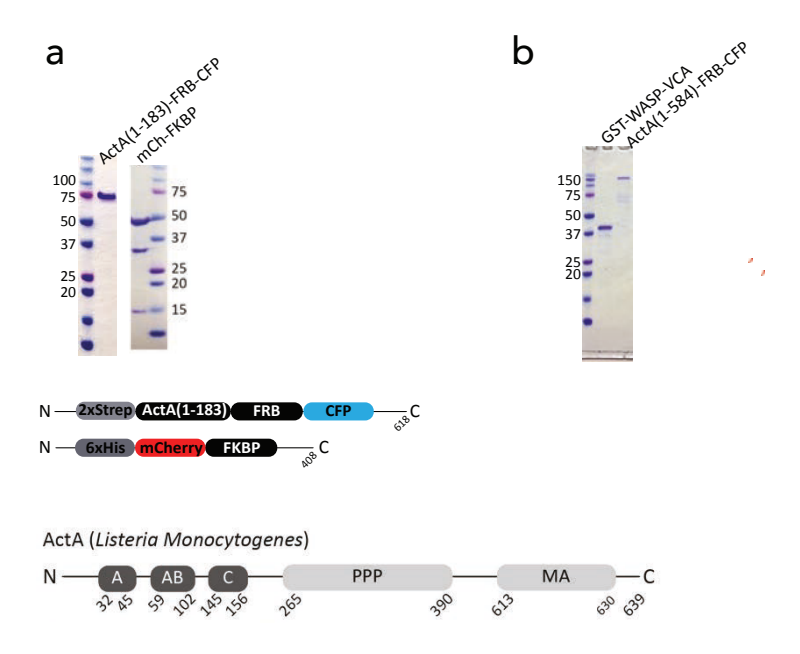
Supplementary Figure 1. Reconstitution of chemical sensing inside GUVs. a. Schematic of the reconstitution of FKBP and FRB fused with YFP and CFP tags. This protein pair heterodimerizes in the presence of 100 μM rapamycin resulting in FRET signal increase. b. Epi-fluorescence images of purified CFP-FRB [$3.2~\mu M$] and YFP-FKBP [$3.2~\mu M$] proteins diffuse in the lumen of the symmetric egg-PC GUVs which form a complex in the presence of rapamycin as indicated by FRET increase. Rapamycin administration resulted in losing the right non-tethered GUV from the field of view. Scale bar is $20~\mu m$. c. Kinetics of the FRET signal normalized by the donor intensity, highlights FKBP-FRB dimerization in the presence of rapamycin but not the DMSO vehicle. n=35 for rapamycin and n=10 for the DMSO conditions. Error bars represent SDs. Luminal fluorescence intensity of the mCherry-FKBP-MARCKS normalized by the average of the initial values prior to rapamycin treatment shows that due to membrane-anchoring, the localization remains unchanged. d. FRET signal for various concentrations of the rapamycin highlights more robust FRET signal with higher rapamycin concentrations. n=14 for both rapamycin and DMSO conditions. Error bars represent SDs.



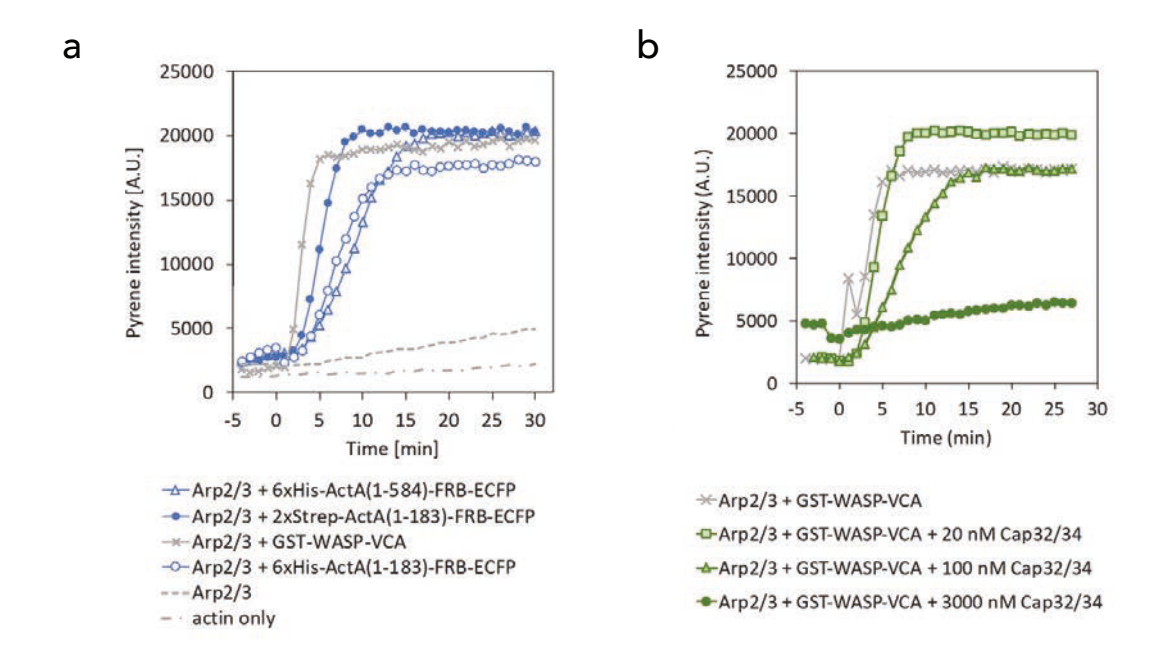


100% Egg-PC lipids

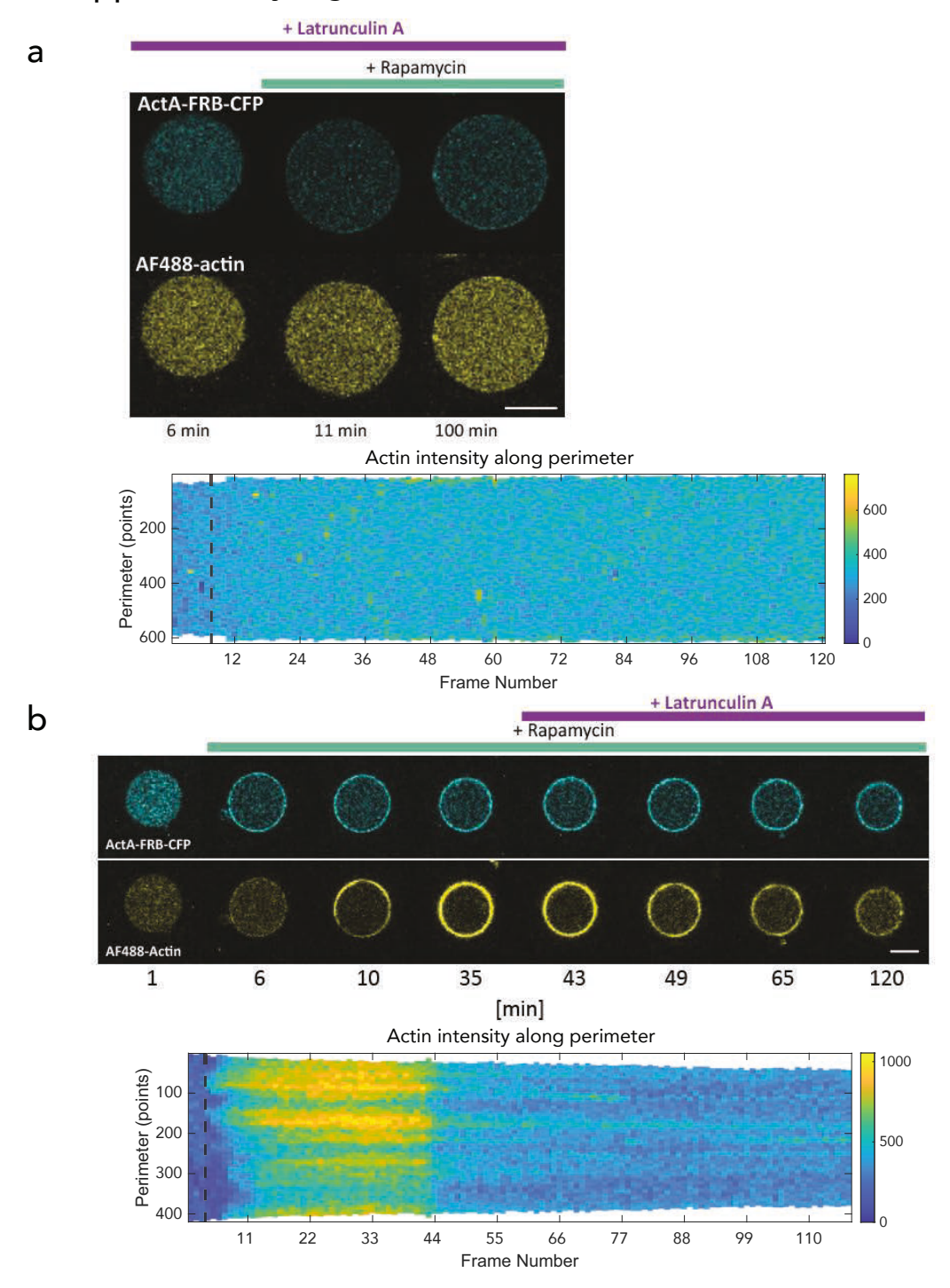
Supplementary Figure 2. MARCKS-tagged protein constructs do not exhibit affinity for PC lipids.



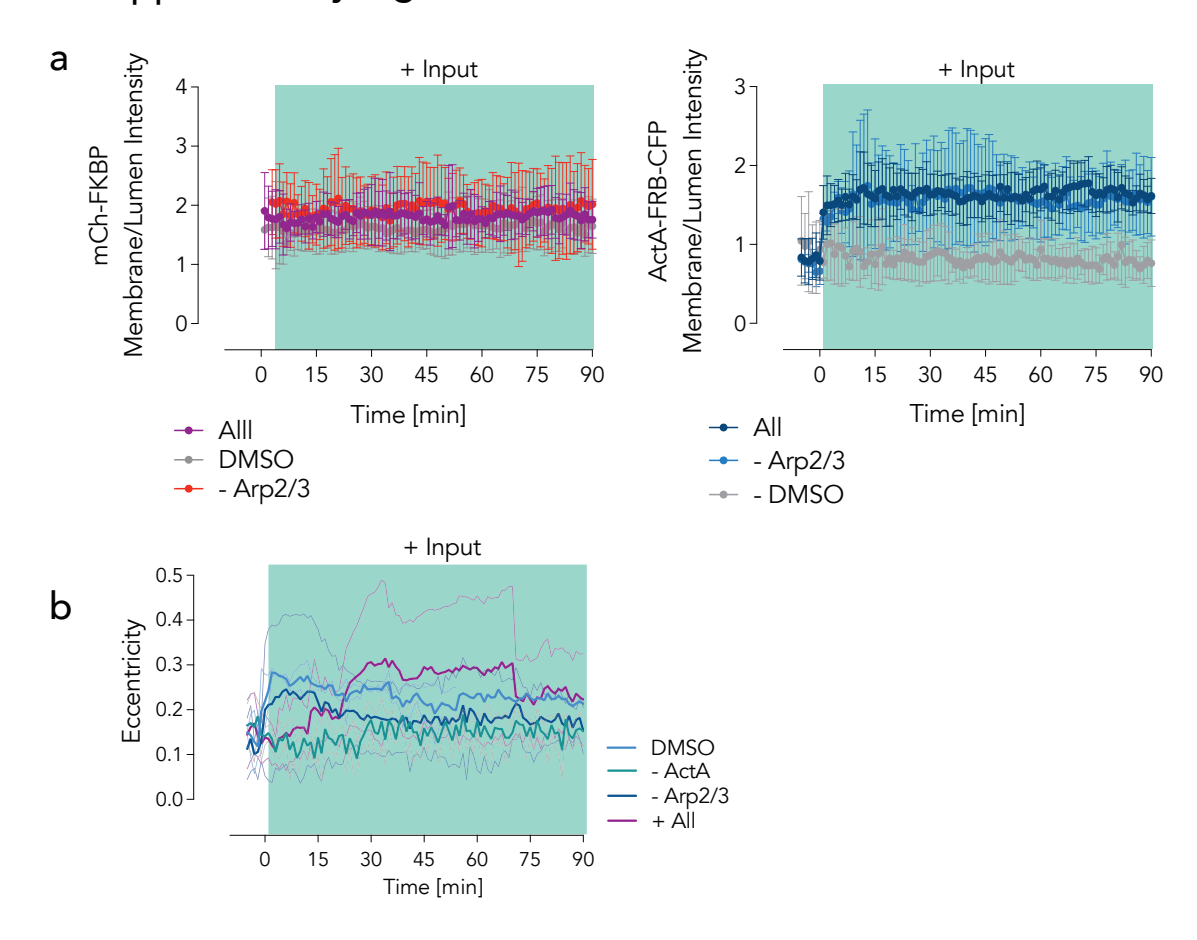
Supplementary Figure 3. Protein purification SDS-PAGE gels. **a.** 6xHis-mCh-FKBP and ActA(1-183)-FRB-CFP purified for the CID experiments. **b.** Purified GST-WASP-VCA (purchased from Cytoskeleton) and ActA(1-584)-FRB-CFP used in the pyrene assay.



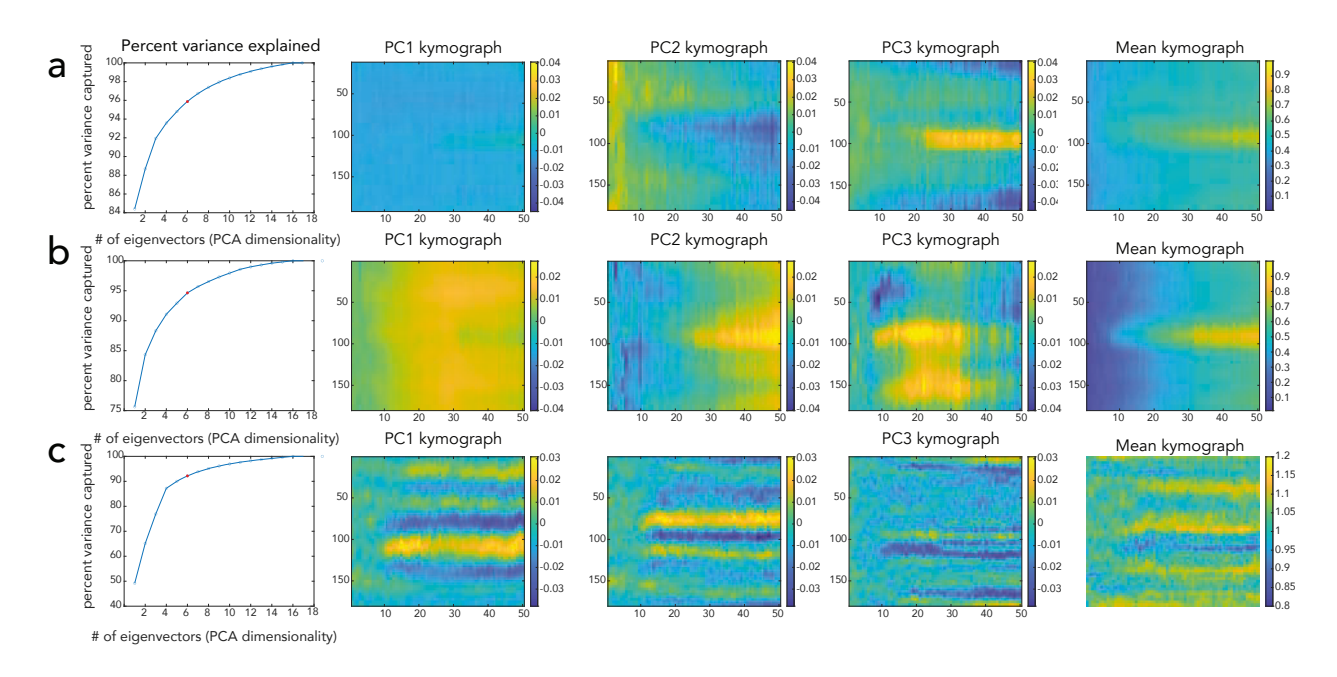
Supplementary Figure 4. In vitro actin polymerization activity of ActA. a. Pyrene actin assay was carried out to assess actin nucleation promoting factor function of purified ActA. ActA(1-584) and ActA(1-183) and its different purification tag variants were tested for their activity with GST-WASP-VCA as a positive control. The data showed similar activities for all ActA variants. Reaction was started with 1 μ M actin in F-buffer. Arp2/3 (final 10 nM) and GST-WASP-VCA or ActA variants (final 800 nM) were added at time = 0. b. Activity of purified cap32/34 was evaluated in pyrene actin assay. Cap32/34 reduced actin polymerization rate and the plateau value of F-actin in a dose-dependent manner. Reaction started with 1 μ M actin with or without cap32/34 in F-buffer and Arp2/3 (final 10 nM) and GST-WASP-VCA (final 800 nM) were added at time=0.



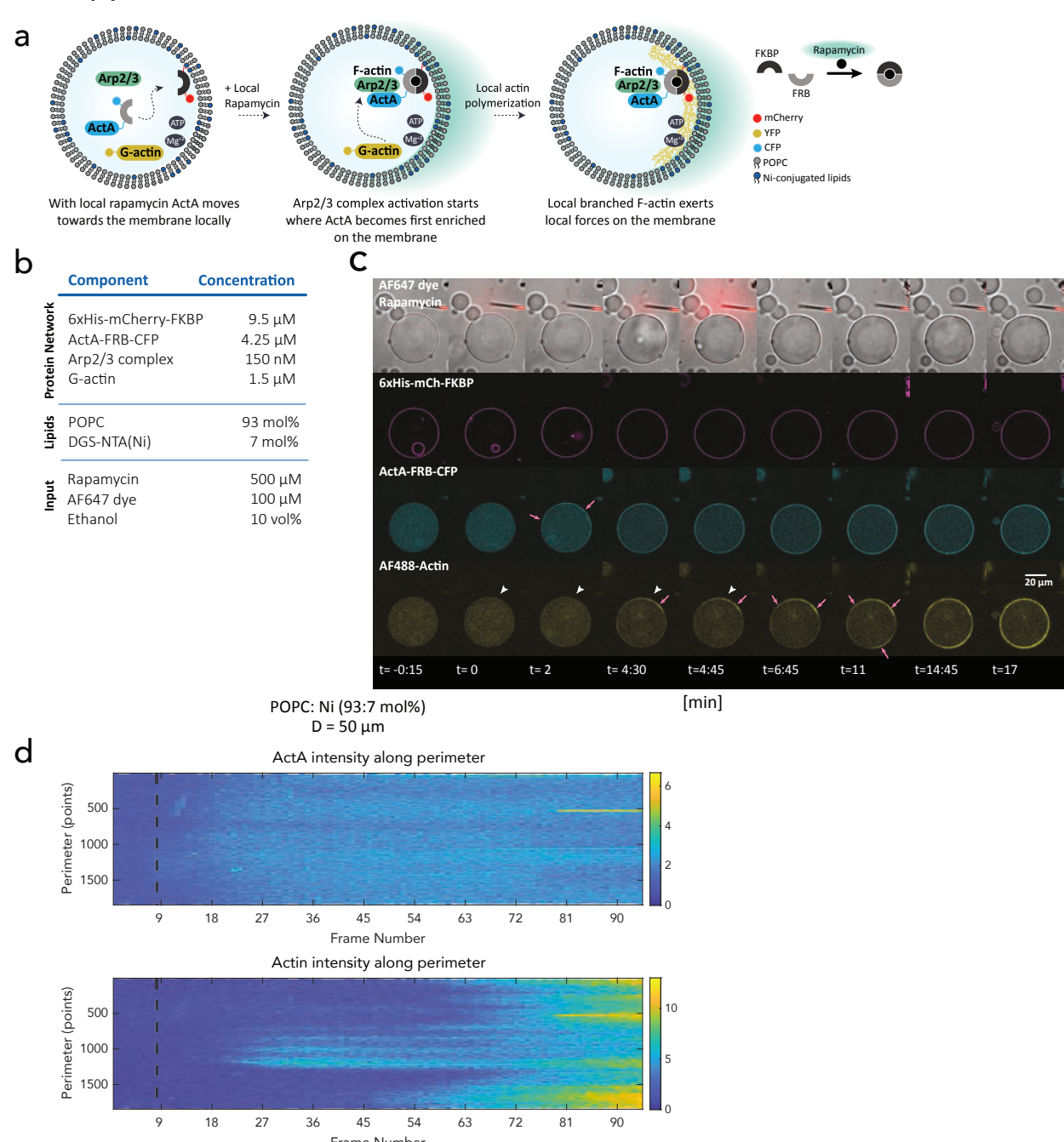
Supplementary Figure 5. Latrunculin administration identifies F-actin on the membrane. **a.** With 5 μM Latrunculin present, actin does not polymerize on the membrane despite ActA recruitment in the presence of rapamycin. **b.** Alternatively, Latrunculin dissociates the already present F-actin on the membrane.



Supplementary Figure 6. CID-induced ActA translation towards the membrane. **a.** ActA signal increases on the plasma membrane after rapamycin administration in the presence or absence of Arp2/3 complex, whereas the mCh-FKBP remains membrane-bound throughout the experiment. **b.** The eccentricity of the GUVs change in response to rapamycin only when all the protein components including ActA, Arp2/3, and actin are present in the system.



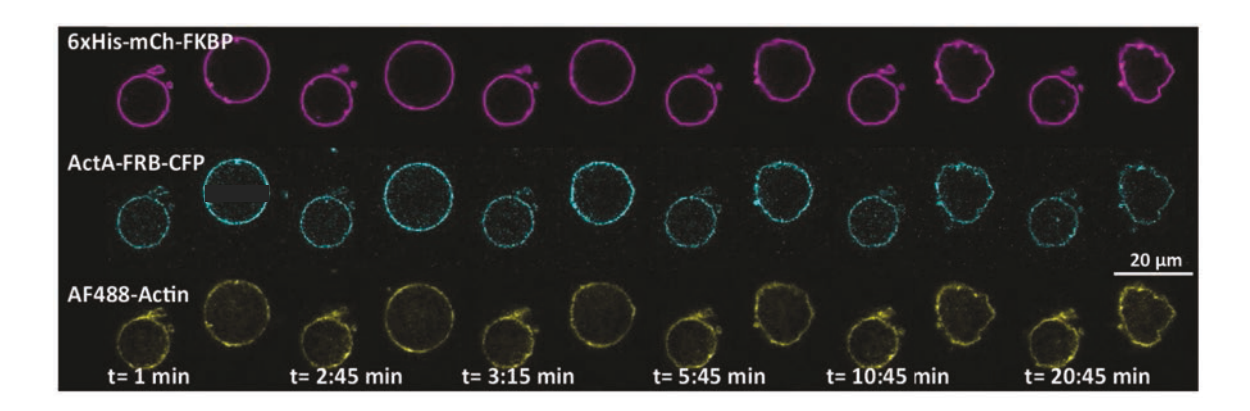
Supplementary Figure 7. Principal component analysis (PCA) on the kymographs to extract dominant modes of spatiotemporal dynamics. **a.** PCA performed on ActA kymographs, max-normalized, and aligned based on the actin kymographs at peak actin signal at 35 frames post-rapamycin addition. The top 3 principal components (PCs) capture over 90% of the variance in the dataset. PC1 kymograph represents the dominant spatiotemporal features, followed by PC2, and PC3, relative to the mean kymograph shown. **b.** The same analysis is applied to the actin and **c.** raw curvature kymographs to identify the key spatiotemporal features in actin distribution and local shape changes. n=17 for all panels.

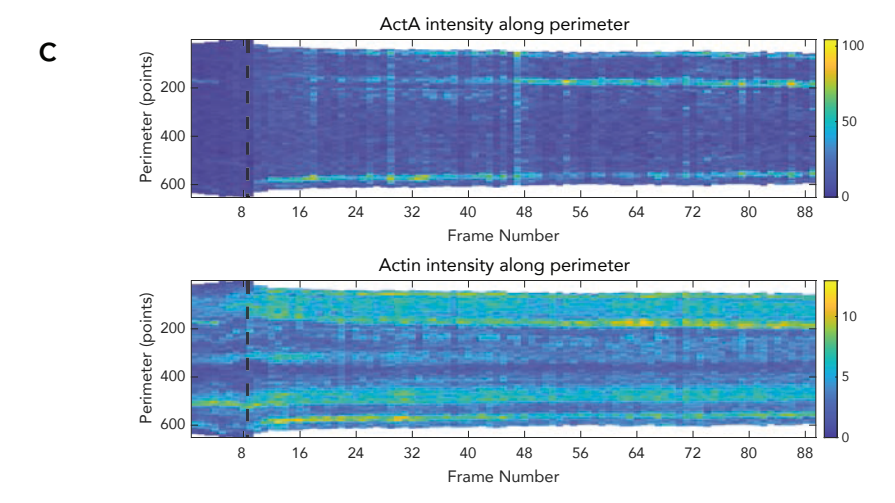


Supplementary Figure 8. Local administration of rapamycin for POPC GUVs. **a.** Cartoon depicting a design whereby ActA can translocate locally in response to a rapamycin input, leading to local actin polymerization. **b.** The components assembled in GUVs to mediate local actin polymerization. **c.** With a local rapamycin input, ActA translocated locally and F-actin polymerization initiated next to the rapamycin source, however due to high lipid diffusion ActA and F-actin distribution did not retain their locality. **d.** Kymograph depicting the distribution of ActA and actin on the membrane preand post- rapamycin addition.

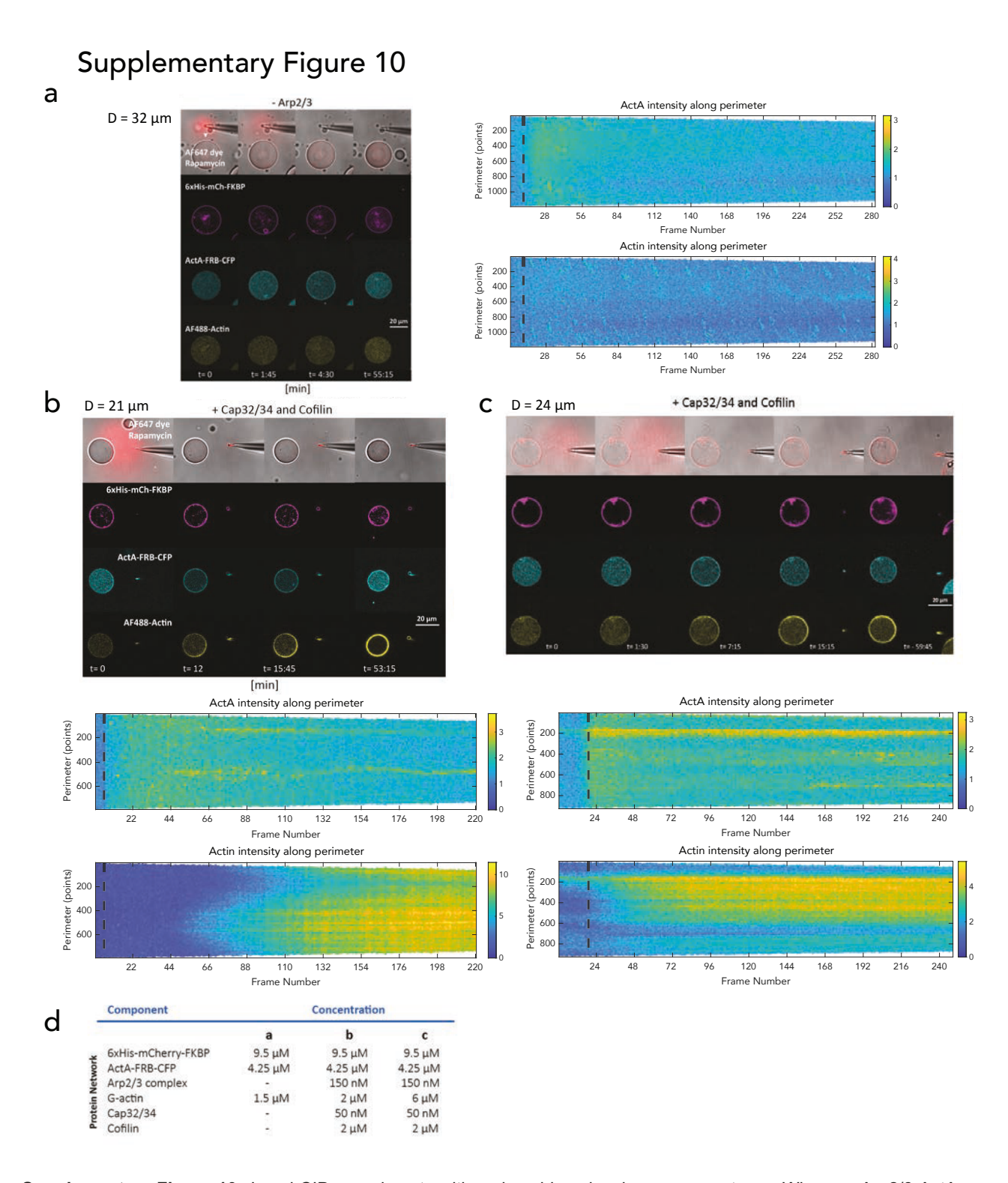
а		Component	Concentration
	Protein Network	6xHis-mCherry-FKE ActA-FRB-CFP Arp2/3 complex G-actin	9.5 μM 4.25 μM 150 nM 1.5 μM
	Lipids	DPPC DGS-NTA(Ni)	93 mol% 7 mol%

b

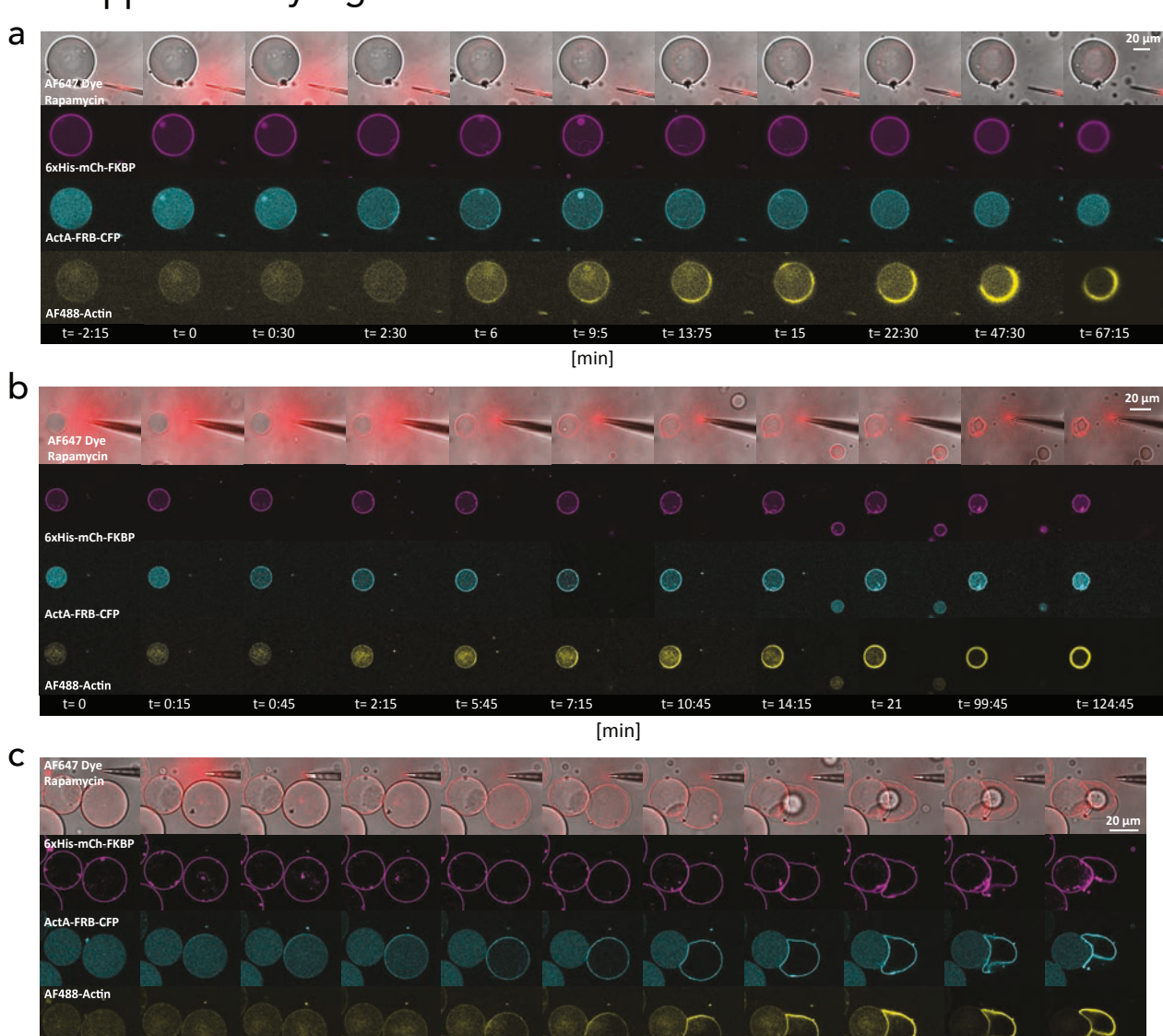




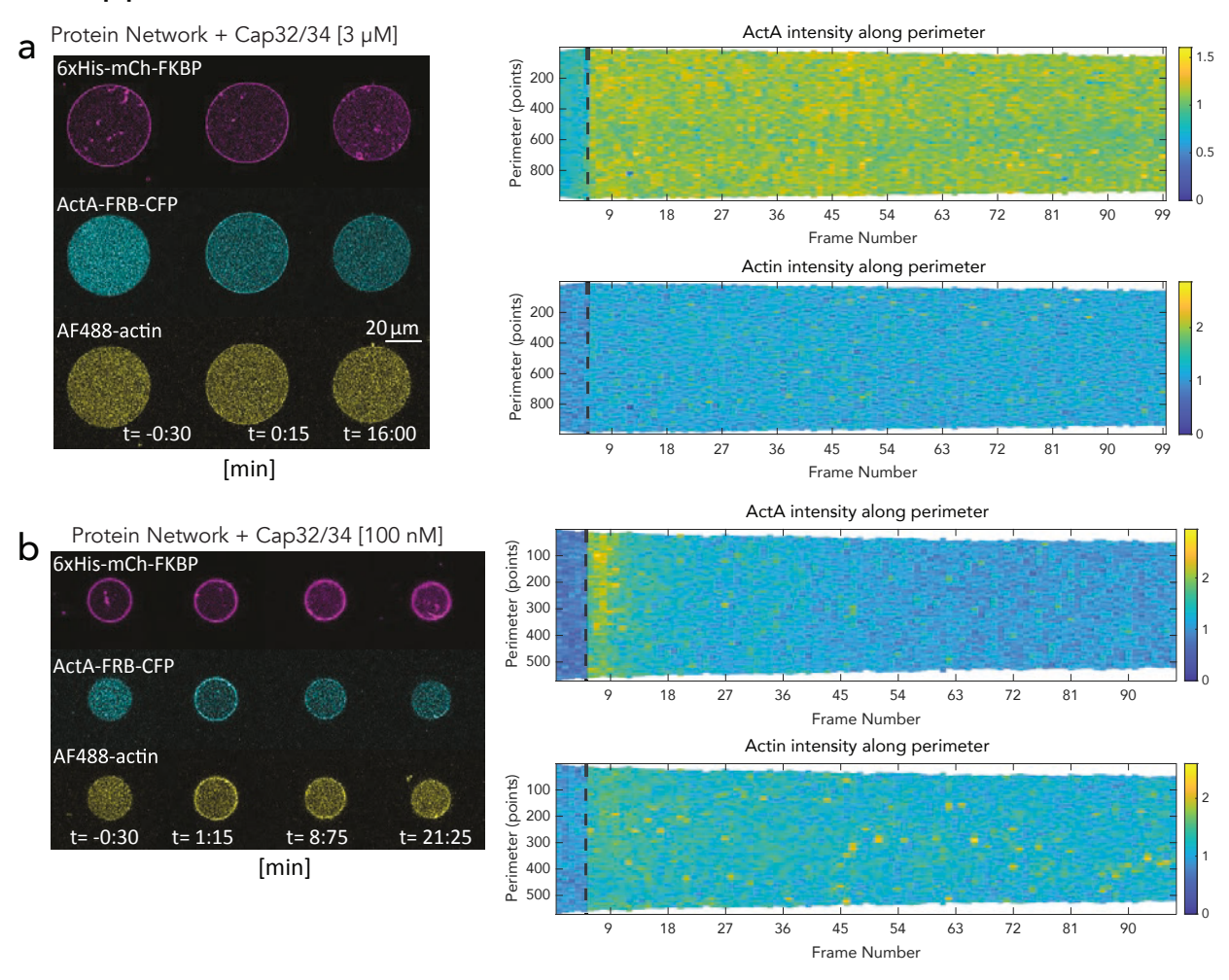
Supplementary Figure 9. Global administration of rapamycin for DPPC GUVs. **a.** Assembled GUVs with DPPC lipids and the biomolecules presented. **b.** The more rigid DPPC containing GUVs deformed as a result of actin polymerization on the membrane. **c.** ActA and actin kymographs, depicting the intensity evolution of each on the membrane for the right, larger GUV on (b).



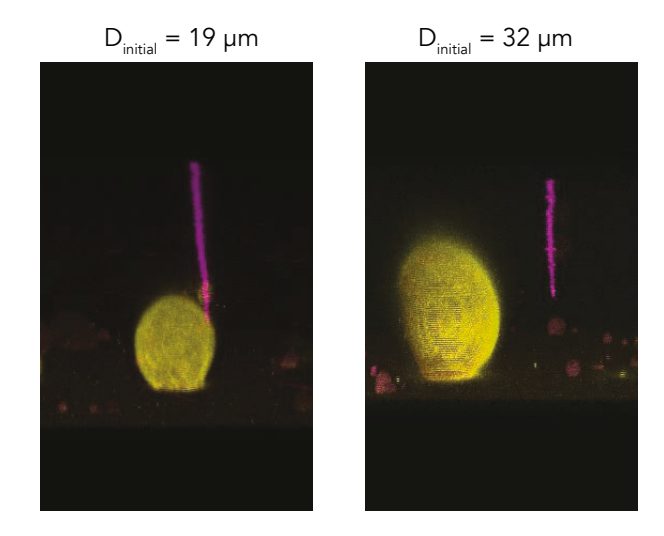
Supplementary Figure 10. Local CID experiments with various biomolecular components. **a.** When no Arp2/3 ActA translocation took place, actin did not polymerize. (**b.-d.**) In the presence of various concentrations of capping protein, cofilin, and actin, the local actin polymerization feature was abolished.



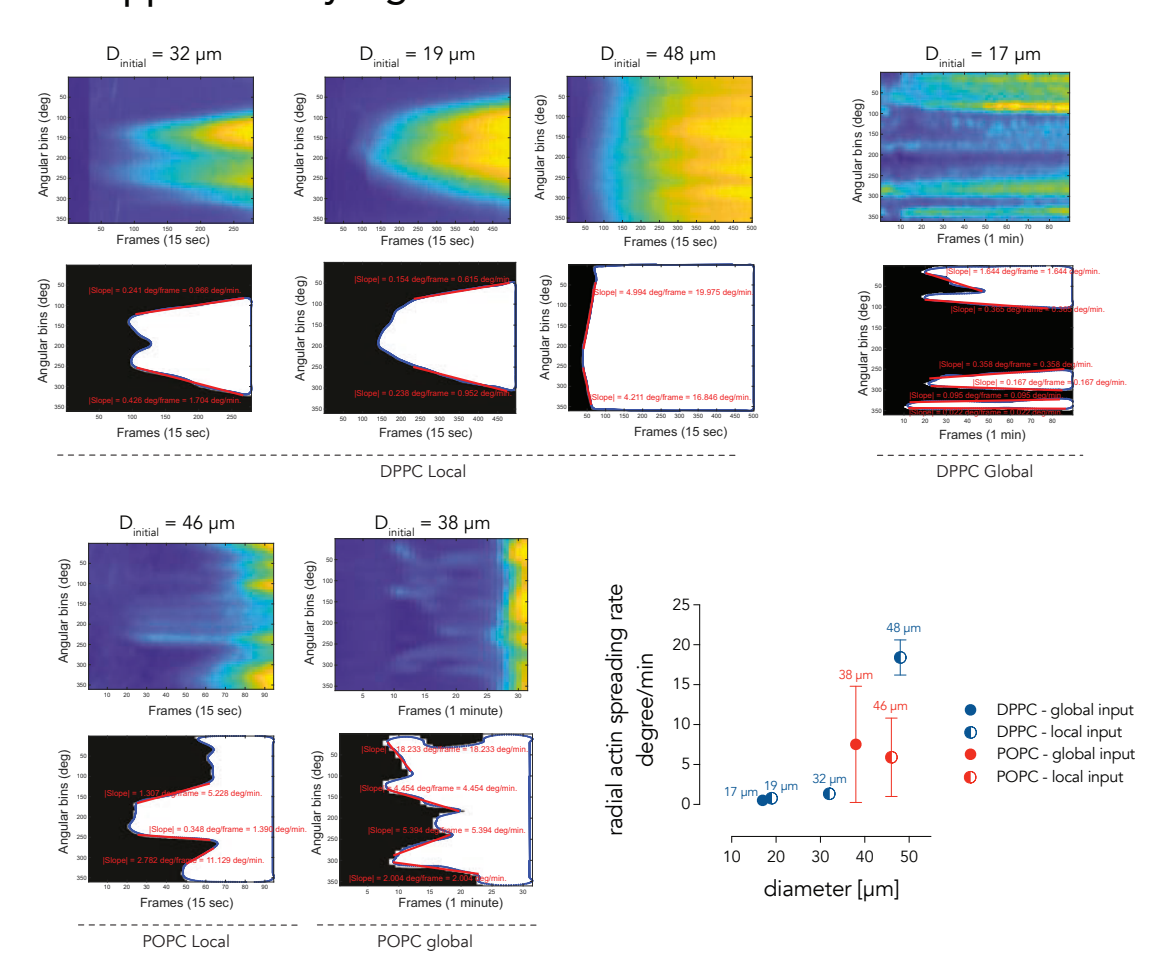
Supplementary Figure 11. Representative Local CID experiments. (a.-c.) Representative images obtained from the local CID experiments (Fig. 5).



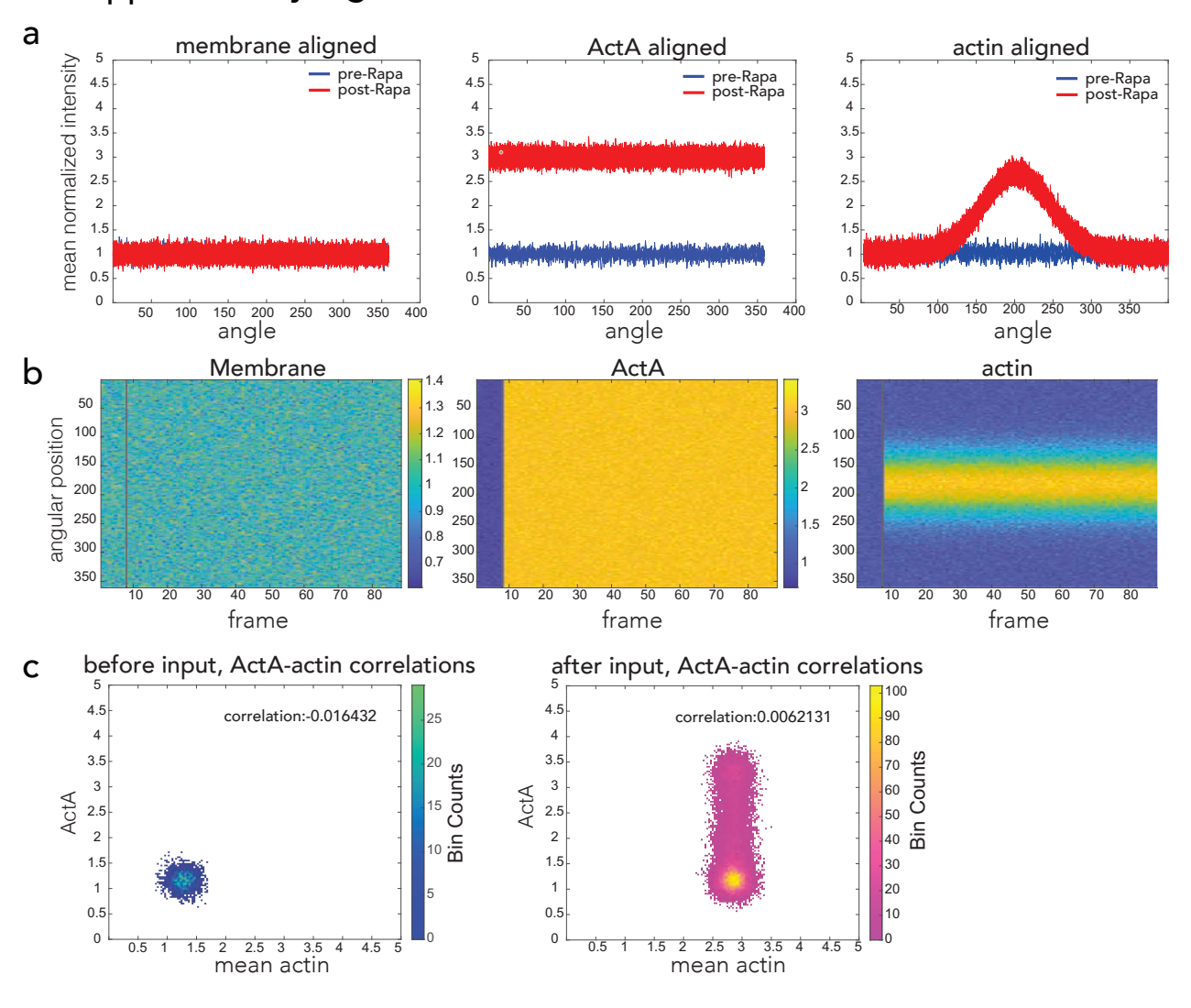
Supplementary Figure 12. Cap32/34 and cofilin abolished actin thickening. **a.** Bulk adminstration of rapamycin for GUVs prepared with 3 μM Cap32/34. **b.** Bulk administration of rapamycin for GUVs prepared with 100 nM Cap32/34.



Supplementary Figure 13. 3D confocal stacks of GUVs post directed rapamycin input administration. The magenta color marks the rapamycin-loaded needle position.



Supplementary Figure 14. Assessment of the radial actin spreading rate for GUVs of POPC vs. DPPC lipid composition in response to undirected and direct actin signal.



Supplementary Figure 15. Assessing our image analysis pipeline against a previously published symmetry breaking report.⁵¹ **a.** Membrane, ActA and actin traces on the GUV boundary before and after actin polymerization on the membrane. **b.** Distribution of membrane, ActA, and actin intensity on the GUV boundary before and after symmetry breaking. **c.** Correlation analysis between ActA and actin before and after actin polymerization on the membrane, highlighting decrease in the Pearson correlation value after actin polymerization induction.

Supplementary Tables

Supplementary Table 1

Table 1 | Lipid composition of the protocells

Figure Number	Leaflet	Lipid	Fatty acid	mol%
Fig. 1	inner	POPC	16:0-18:1	80
		POPS	16:0-18:1	20
	outer	Egg-PC	N/A	80
		POPS	16:0-18:1	20
Figs. 2, 3, Supps. Figs. 4-6, 11	inner/outer	POPC	16:0-18:1	94
		DGS-NTA(Ni)	18:1-18:1	5
		PEG2000 PE	16:0-16:0	1
Fig. 5, Supp. Figs. 8-10	inner/outer	DPPC	18:0-18:0	93
		DGS-NTA(Ni)	18:1-18:1	7
Supp. Fig. 1	inner/outer	Egg-PC	NA	100
Supp. Fig. 7	inner/outer	POPC	16:0-18:1	93
		DGS-NTA(Ni)	18:1-18:1	7

POPC: 1-palmitoyl-2-oleyl-sn-glycero-3-phosphocholine POPS: 1-palmitoyl-2-oleoyl-sn-glycero-3-phospho-L-serine

Egg PC: L-α-phosphatidylcholine (Egg, Chicken)

DGS-NTA(Ni): 1,2-dioleoyl-sn-glycero-3-[(N-(5-amino-1-carboxypentyl)iminodiacetic acid)succinyl] PEG2000 PE: 1,2-dipalmitoyl-sn-glycero-3-phosphoethanolamine-N-[methoxy(polyethylene glycol)-2000]

Supplementary Table 1. Lipid composition of the protocells fabricated for various experimental conditions.

Supplementary Table 2

Global

_	Component	Concentration
Protein Network	6xHis-mCherry-FKB ActA-FRB-CFP Arp2/3 complex G-actin	P 9.5 μM 8.5 μM 150 nM 1.5 μM
Lipids	POPC DGS-NTA(Ni) PEG	94 mol% 4 mol% 1 mol%

Local

	Component	Concentration
Protein Network	6xHis-mCherry-FKE ActA-FRB-CFP Arp2/3 complex G-actin	8P 9.5 μM 4.25 μM 150 nM 1.5 μM
Lipids	DPPC DGS-NTA(Ni)	93 mol% 7 mol%
Input	Rapamycin AF647 dye Ethanol	500 μM 100 μM 10 vol%

Supplementary Table 2. Molecular constituents of the protocells used in bulk versus local CID experiments.

Supplementary Movies 1 to 3 captions

Movie S1. Time-lapse images of the CFP-FRB translocation towards mCh-FKBP-MARCKS upon rapamycin administration.

Movie S2. Time-lapse images of rapamycin-induced global ActA translocation towards the membrane and the ensuing actin polymerization that deforms the membrane into an asymmetric shape.

Movie S3. Time-lapse images of rapamycin-induced localized ActA translocation towards the membrane and the ensuing local actin polymerization.